Destroy, create, transform and sublimate: laboratory dissociation studies on polycyclic aromatic hydrocarbons and analogues

Kamer, J.

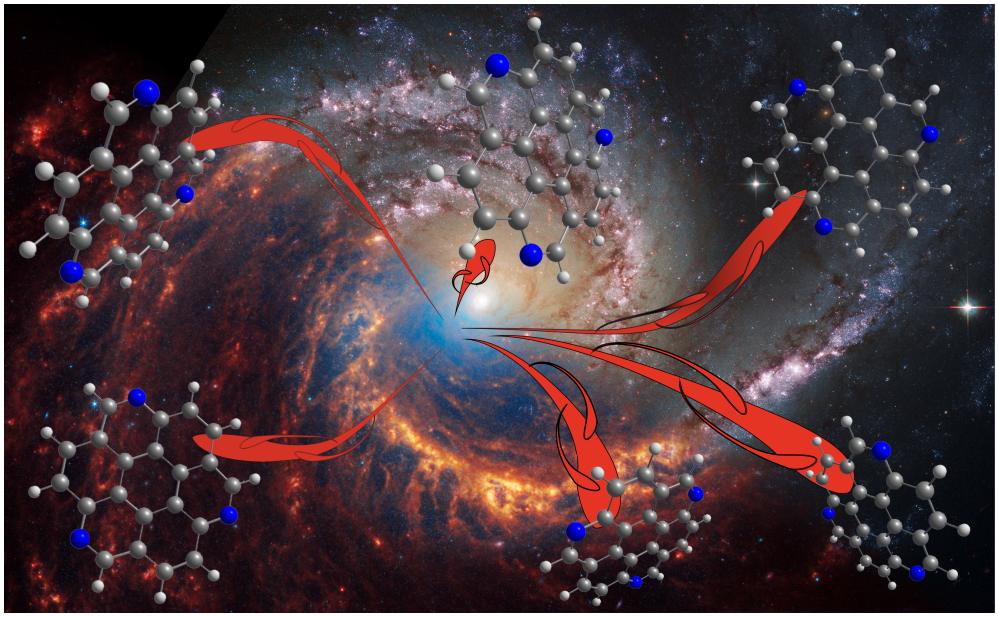

5 Photoprocessing of Cationic Triazacoronene: Dissociation Characteristics of Polycyclic Aromatic Nitrogen Heterocycles in Interstellar Environments

Polycyclic aromatic nitrogen heterocycles (PANHs) are present in various astronomical environments where they are subjected to intense radiation. Their photodissociation pathways give crucial insights into the cycle of matter in the universe, yet so far only the dissociation characteristics of few PANHs have been investigated. Moreover, most experiments use single photon techniques that only reveal the initial dissociation step, and are thus unsuited to replicate astronomical environments and timescales. In this work, we use the Instrument for the Photodynamics of PAHs (i-PoP) at the Laboratory for Astrophysics to simulate the interstellar photodissociation of a model PANH, cationic triazacoronene (**TAC**$^{\bullet+}$, $C_{21}H_9N_3$). Comparing the observed fragments to similar PAHs such as the isoelectronic coronene can give mechanistic insight into PAH dissociation. For coronene the major photodissociation products were found to be C_9H^+, $C_{10}{}^+$, and $C_{11}{}^+$. In contrast, fragmentation in **TAC**$^{\bullet+}$ is initiated by up to three HCN losses often in combination with H- or H_2 losses. In the lower mass region, the fragments show similarities to comparable PAHs like coronene, but for **TAC**$^{\bullet+}$ the inclusion of nitrogen atoms into the ionic fragments in the form of e.g. (di)cyanopolyynes is also observed. These nitrogen-containing species may be important tracers of regions in interstellar space where interstellar PANHs are being photodissociated.

Schleier, D., Kamer, J., Jiao, A., Schneider, G. F., Linnartz, H., Bouwman, J., 2024, Physical Chemistry Chemical Physics, 26, 15547-15558.

5.1 Introduction

Polycyclic aromatic hydrocarbons (PAHs) are ubiquitous in various regions in the interstellar medium (ISM) and planetary atmospheres, such as that of Saturn's largest moon, Titan (Tielens 2008; López-Puertas *et al.* 2013; Delitsky & McKay 2010). In the ISM, they are identified based on their characteristic mid-infrared (mid-IR) emission bands that arise when PAHs cascade down to the ground state after getting excited by the interstellar radiation field (Allamandola *et al.* 1985, 1989; Leger & Puget 1984; Dale *et al.* 2023; Chown *et al.* 2024). The 6.2 μm features of PAHs are consistently red-shifted compared to the observed IR emission bands and thus homocyclic PAHs alone cannot explain the observations (Peeters *et al.* 2002; Hudgins *et al.* 2005). Heteroatom substitutions were proposed to account for this observed shift in position of the 6.2 μm emission feature (Ricca *et al.* 2021). Recent experimental studies have confirmed that incorporating nitrogen atoms into the PAH honeycomb structure indeed shifts the IR features towards shorter wavelengths (Rap *et al.* 2022), but this shift is only noticeable for endoskeletal nitrogen atoms, in which a carbon atom inside the molecule is replaced by a nitrogen atom. The relative abundance of interstellar endoskeletal polycyclic aromatic nitrogen heterocycles (PANHs) has recently been estimated to be no more than 12% (Ricca *et al.* 2021). Exoskeletal substitutions, i.e. a CH/N exchange, hardly alter the IR emissions and, thus, exoskeletal PANHs may contribute significantly to the observed emission bands.

Based on the molecular heat capacity it is believed that only large PA(N)Hs with more than 50 heavy atoms survive the harsh interstellar radiation field (Allamandola *et al.* 1989; Tielens 2008; Allain *et al.* 1996). Smaller PA(N)Hs get photoprocessed on astronomical time scales and fragment into thermodynamically more stable species. The dissociation of several model PAHs, such as dicoronylene, dibenzopyrenes (Hrodmarsson *et al.* 2022, 2023), naphthalene (Bouwman *et al.* 2016), and anthracene (Banhatti *et al.* 2022) have been studied experimentally in detail. In catacondensed PAHs like dibenzopyrenes the inital dehydrogenation is always accompanied by the loss of acetylene (C_2H_2) fragments, whereas H-loss dominates for more symmetrical PAHs like coronene and dicoronylene (Ekern *et al.* 1998; Panchagnula *et al.* 2024). Subsequently, different carbon clusters and polyyne chains are formed, which can also contain a small number of hydrogen atoms. Among those carbon clusters, C_{11}^+ is one of the most intense and it is thus believed that it represents a thermodynamic sink (Hrodmarsson *et al.* 2022, 2023; Panchagnula *et al.* 2024).

Just like PAHs, PANHs may also show universal fragmentation pathways that lead to common photoproducts from different parent molecules (Subramani *et al.* 2023). Although significant efforts have been put into elucidating the dissociation characteristics of PAHs, very little is known about those for PANHs. Bouwman *et al.* (2015) investigated the dissociation of quinoline and isoquinoline cations by dissociative photoionization (DPI) and found nearly isoenergetic channels H-loss and HCN-loss. The dissociation barriers are almost 1 eV lower when compared to similar channels in naphthalene, signaling that nitrogen incorporation into a PAH framework lowers its stability. A similar observation was made in phenantridine and acridine ($C_{13}H_9N$) which exhibit the loss of a HCN fragment upon electron ionization resulting in the introduction of five-membered rings in the nascent PAH structure (de Haas *et al.* 2017). Based on these studies it is currently believed that PANHs initially eliminate all nitrogen atoms through HCN losses and eventually turn into pure PAHs. Yet, due to the nature of these single step dissociative ionization experiments, only the initial dissociation pathways are revealed and as such they fail to give a complete picture of processing of PAHs on longer, astronomically more relevant, time scales. In addition, the investigated PANHs only contain a single nitrogen atom and are limited to a maximum of three aromatic cycles, while interstellar PAHs are believed to be larger with potentially more than one hetero atom substitution.

Here, we use the instrument for the Photodynamics of PAHs (i-PoP) to investigate the

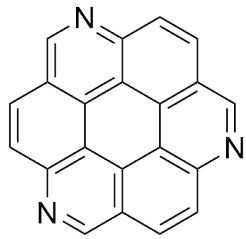

Figure 5.1: Structure of the investigated Triazacoronene.

similarities and dissimilarities in the photoprocessing of PAHs and PANHs. This setup has been used in the past to study infrared spectroscopic properties of PAHs (Zhen *et al.* 2017, 2018; Bouwman *et al.* 2019, 2020, 2021) as well as various facets of PAH photoprocessing (Zhen *et al.* 2014a,b; Castellanos, P. *et al.* 2018; Zhang *et al.* 2019, 2023; Hrodmarsson *et al.* 2022, 2023; Panchagnula *et al.* 2024). As a model compound for our study we chose 1,5,9-triazacoronene (**TAC**, $C_{21}H_9N_3$, illustrated in Fig. 5.1). **TAC** is a structural variation of coronene in which three equidistant CH-groups are replaced by three nitrogen atoms. Coronene is a highly symmetric pericondensed PAH, which has been studied in the past (Simon *et al.* 2017; Chen *et al.* 2020). **TAC** contains about twice the number of heavy atoms (C, N) compared to the previously largest investigated PANHs and is thus of larger interstellar significance. Moreover, its dissociation may result in the incorporation of one or more nitrogen atoms in the fragment ions. The isoelectronic CH/N exchange shifts their mass up by 1 atomic mass unit (amu) per nitrogen atom (i.e. 3 amu for **TAC**).

5.2 Methods

The experiments on the dissociation of $\mathbf{TAC}^{\bullet+}$ were performed on i-PoP, situated in the Laboratory for Astrophysics (LfA) at Leiden Observatory. **TAC** was synthesized according to a procedure described in the literature (Tan *et al.* 2016). The complete synthesis procedure, including NMR spectroscopic data can be found in the appendix. The experimental apparatus has been described in detail elsewhere (Zhen *et al.* 2014a), so only a brief description is given here.

The setup consists of two differentially pumped chambers; a source chamber that houses a commercial ion trap (Jordan C-1251), and a detection chamber which comprises a reflectron time-of-flight (re-TOF) spectrometer (Jordan D-850). The samples were placed in an oven (Heat Wave Labs) that is positioned in the source chamber next to the ion trap and heated to 150°C to gently sublimate the **TAC** sample.

The neutral molecules that sublimated from the oven were ionized by electron ionization at 70 eV using an electron gun (EGUN, Jordan C-950). The formed cations were subsequently guided into the ion trap through electrostatic lenses and an ion gate that determines the fill time of the trap. The ions were captured in the 1 MHz radio frequency (RF) field of the trap and the ion cloud was confined to the center of the trap by admitting a small, continuous flow of helium gas to the ion trap assembly reaching a static pressure of $1 - 2 \times 10^{-6}$ was reached in the source chamber. The RF amplitude was set to 1500 V and resulted in trapping of ions with mass to charge ratios (m/z) down to 93. However, the signals of lowest masses from m/z 93 to 103 were found to fluctuate and were disregarded in the analysis.

The data acquisition scheme can be separated into four distinct steps that are described in this paragraph. First, the ion trap was filled for 2.7 s, after which the ion gate was closed. A Stored Waveform Inverse Fourier Transform (SWIFT) pulse of 0.25 s was applied to one of the end caps of the ion trap to filter out all of the ions but the ionic species of interest,

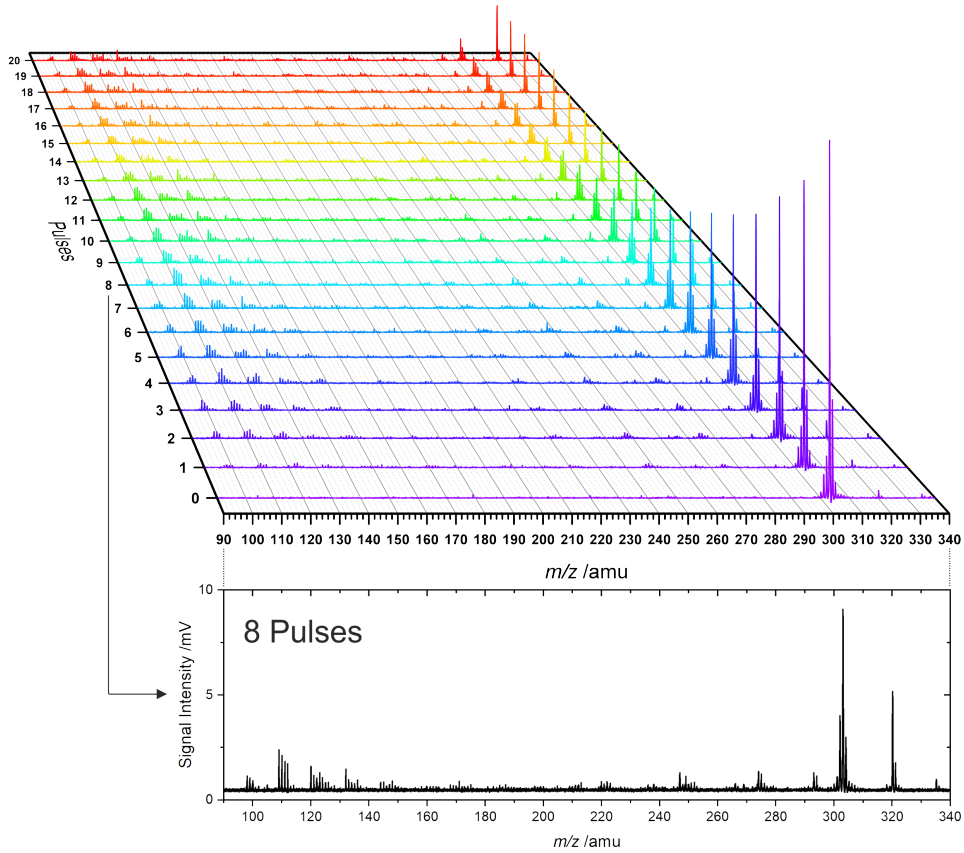

Figure 5.2: Photodissociation mass spectra for $\mathbf{TAC}^{\bullet+}$ as a function of the number of applied laser pulses (fluence). A 2D mass spectrum after 8 pulses is displayed at the bottom.

which in our case is $\mathbf{TAC}^{\bullet+}$. After a brief re-thermalization period (0.05 s) the isolated ions inside the trap were exposed to laser light from a dye laser (LIOP-TEC, Quasar2-VN) that was pumped by a 10 Hz Nd:YAG (INDI-40-10). The dye laser was filled with the dye 4-(dicyanomethylene)-2-methyl-6-(4-dimethylaminostyryl)-4H-pyran (DCM) dissolved in ethanol and tuned to a wavelength of 630 nm. This wavelength allows to utilize a multi-photon absorption approach, which helps to probe the potential energy surface of $\mathbf{TAC}^{\bullet+}$ more gently, with respect to its dissociation barriers. It also limits secondary processes, like multiple ionization, which has been observed in experiments with VUV photons and PAHs of similar sizes, among them coronene (Zhen *et al.* 2016; Wenzel *et al.* 2020). The laser pulse energy measured outside the vacuum chamber after passing through the ion trap was set to 4.1 mJ and the laser pulse has a duration of 10 ns with a diameter of 1.2 ± 0.1 mm, resulting in an average fluence of 362.5 mJ cm^{-2} pulse^{-1}. The number of laser pulses admitted to the ion cloud in the trap ranged from 0 to 20 and was controlled by a mechanical shutter. The exposure to laser light is expressed as fluence (number of pulses $\times$ laser pulse energy). During the irradiation period, the ions were always retained for a the same amount of time, typically two seconds, independent of the number of laser pulses that they were subjected to. In the final step, a potential of ~ -800 and $\sim +800$ V was applied to the end cap electrodes of the ion trap to accelerate the ions into the reflectron time-of-flight (re-TOF) tube. Ions were detected using a multichannel plate (MCP) detector and digitized using an 8-bit GaGe Cobra card. The aforementioned data acquisition sequence was programmed in a LabVIEW routine that controlled two high-precision delay generator (SRS DG535) via a GPIB interface. The measurement routine was triggered on the signal of the Q-switch of a Nd:YAG laser to ensure exposure to the correct number of laser pulses during each measurement cycle. Each mass spectrum for a certain laser exposure was taken as an average over 50 individual mass spectra.

In order to quantitatively investigate the data, each peak was fitted with a Pearson type IV distribution (Pearson 1895) to account for the asymmetry in the mass peak (see Fig. 5.19 in the appendix for a typical fit). Subsequently, the fitted distribution was integrated numerically, giving the integrated signal intensity of the mass peak. The integrated intensities for each peak were normalized to the parent $\mathbf{TAC}^{\bullet+}$ signal at zero pulses and corrected for ^{13}C contributions.

Experimental errors were determined from the fluctuations in the ion signal at each normalization measurement, which was found to fluctuate by a total of 15%. These errors can only be given on a measurement-to-measurement basis, but each peak in a mass spectrum should be equally affected by the filling of the ion trap. Errors of the fitting procedure were accounted for by introducing a random noise signal for each peak using the Markov Chain Monte Carlo (MCMC) method. Each peak was subsequently refitted, giving the total error of the fit for each peak. The total error of the fit is far below 1%, resulting in a combined relative error of 15%.

5.3 Results

An overview of the mass spectra range as a function of laser fluence is given in Fig. 5.2. The formed ionic dissociation products are discussed in the following sections for three mass ranges: high (m/z 300 − 320), medium (m/z 200 − 299) and low (m/z 103 − 199).

5.3.1 Mass range m/z 300 − 320

The most intense peak in the mass spectrum when the ion cloud is not subjected to any laser light is observed at m/z 303 and is attributed to the parent $\mathbf{TAC}^{\bullet+}$. Weak signals are seen at m/z 302 and 301, which correspond to hydrogen loss from the parent ion caused by electron ionization of the parent species, and have relative intensities of 11% and 6%, respectively. The

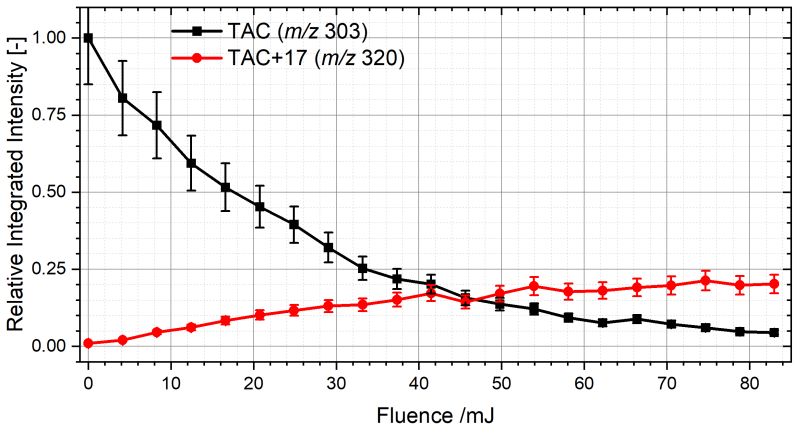

Figure 5.3: Integrated values of all major peaks in the range of m/z 300 – 325 as a function of laser fluence.

signals at m/z 304 and 305 correspond to the ^{13}C isotope peaks and their relative intensities are 25% and 3%, which aligns very well with the expected isotope abundance. These weak signals observed next to the parent ion signal at zero laser pulse exposure cannot be filtered out completely using the SWIFT filtering technique.

After being subjected to an increasing number of laser pulses, a peak at m/z 320 grows in, while the parent signal is depleted. As illustrated in Fig. 5.3 the former is absent when the ions are not exposed to radiation, but continues to grow until the maximum number of pulses has been reached. Hence, this peak is the result of a reaction occurring inside the ion-trap and is likely initiated by photoactivation the parent ion. The most probable reactant is water which is always present in neutral background gas inside our vacuum chamber. However, the direct addition of water to $\mathbf{TAC}^{\bullet+}$ would result in a product at m/z 321. The absence of any reaction when retaining $\mathbf{TAC}^{\bullet+}$ in the ion trap without irradiation, points to a involvement of the hydrogen loss product $\mathbf{TACH}^{+}$ (at m/z 302) and water to form the species at m/z 320. Similar behavior was observed for another nitrogen-containing aromatic molecule, 3-azafluoranthene (Schleier *et al.* 2024b). The loss of a hydrogen atom leads to the formation of a cationic hetero-aryne, which are known to be very reactive even towards closed-shell molecules (Sparrapan *et al.* 2000). To investigate this further we have performed experiments, where we admitted a mix of 5% acetylene in helium to the ion trap. The resulting mass spectrum is given in Fig. 5.20 in the appendix and shows that almost all water addition product is replaced by an acetylene addition product (m/z 328). We recorded a mid-infrared (IR) action spectrum of the m/z 320 species to identify the structure of the water addition product, which indeed corroborates the above conclusion. The mid-IR spectra of the m/z 320 species, as well as $\mathbf{TAC}^{\bullet+}$ and protonated **TAC** are the subject of another manuscript (Kamer *et al.* 2024).

Further hydrogen losses are not observed, as illustrated in Fig. 5.21 in the appendix, likely due to the high reactivity of $\mathbf{TACH}^{+}$.

The integrated signals of both m/z 303 and 320 in Fig. 5.3 show a clear trend that m/z 320 is formed at the expense of the parent $\mathbf{TAC}^{\bullet+}$. After 20 laser pulses the $\mathbf{TAC}^{\bullet+}$ signal is essentially gone, whereas the m/z 320 signal reaches its maximum at about 20% of the original $\mathbf{TAC}^{\bullet+}$ signal making it by far the strongest single product peak in the $\mathbf{TAC}^{\bullet+}$ photolysis.

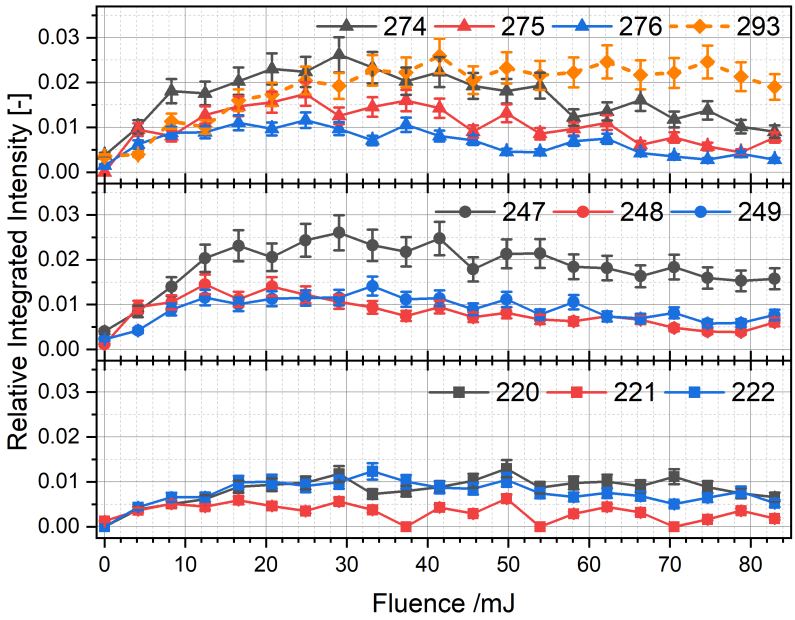

Figure 5.4: Integrated values of all observed peaks in the range of m/z 200 – 299 as a function of laser fluence.

5.3.2 Mass range m/z 200 – 299

In this intermediate mass range, peaks at m/z 293, m/z 294, 274 – 276, 247 – 249, and 220 – 222. The intensity of each peak is about ten times lower than the signal for the water addition product at m/z 320 and less than 3% of the initial $\mathbf{TAC}^{\bullet+}$ signal. With the exception of the first, all of these product ions align with loss of HCN or HCN + H/H_2 from $\mathbf{TAC}^{\bullet+}$. HCN losses are often observed as an initial and low energy decomposition pathway in cationic PANHs (Bouwman *et al.* 2015; de Haas *et al.* 2017).

The integrated signals in this mass range are shown in Fig. 5.4. From this it is clear that all aforementioned species are formed within the first few laser pulses and reach their peak at ∼8 pulses after which they decline steadily. The two most intense peaks are at m/z 274 and 247, which exhibit a mass difference of 27, corresponding to the mass of a HCN fragment. Interestingly, m/z 274 can only originate from $\mathbf{TAC}^{\bullet+}$ via a CNH_3 loss, which could also be a sequential loss of HCN and H_2. The signals at m/z 276, 249 and 222 correspond to the consecutive loss of HCN from $\mathbf{TAC}^{\bullet+}$. Their signals are comparable in integrated intensity for all three over the investigated laser fluences and is about half of the signals at m/z 274 or 247, indicating that the loss of CNH_3 (or HCN + H_2) followed by HCN loss is preferred over the loss of multiple HCN units from the parent $\mathbf{TAC}^{\bullet+}$. The other signals (m/z 275, 248, 221) would correspond to the loss of CNH_2 (or HCN + H) followed by HCN loss and show a similar fluence dependence and comparable intensities to signals at m/z 276, 249 and 222.

The only peak in the intermediate mass range that cannot be explained with the loss of $CNH_{n=1-3}$ from **TAC** is m/z 293. The obvious solution would be the loss of HCN from m/z 320. To confirm this, we generated and subsequently isolated m/z 320 in the ion-trap and irradiated it without any other masses present. The corresponding mass spectra in Fig. 5.22 in the appendix show no visible decay upon irradiation, eliminating the possibility of such a process occurring. Hence, m/z 293 is likely a reaction product forming in the trap. If we again assume that water is the primary reactant, then a CNH_2 loss (or H-loss followed by

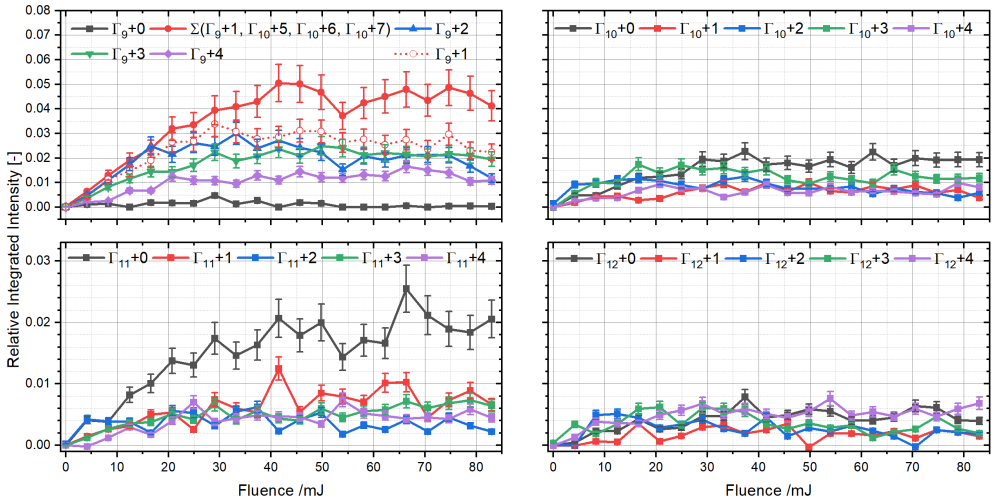

Figure 5.5: Photon flux dependence of individual mass peaks for Γ_9 (top left), Γ_{10} (top right), Γ_{11} (bottom left), and Γ_{12} (bottom right). Due to the reaction of $\Gamma_9 + 1$ with water, its original signal (empty red dots) was modified by adding the $\Gamma_{10} + 5$, $\Gamma_{10} + 6$, and $\Gamma_{10} + 7$ signals.

HCN loss) from $\mathbf{TAC}^{\bullet+}$ with a subsequent water addition could explain the appearance of m/z 293 in a manner analogous to the addition of water to $\mathbf{TACH}^{+}$.

The integrated signals in this mass region indicate that either direct HCN losses from $\mathbf{TAC}^{\bullet+}$ may be less important than CNH_3 (or HCN + 2H) losses, or that fragment ion species formed by direct HCN loss are so unstable that they decompose more readily by also eliminating H, or H_2 fragments.

5.3.3 Mass range m/z 103 – 199

In the lowest mass range, there are not only more but also more intense signals (> 5% of the initial parent signal) compared to the previous region. All detected ion masses in this range are depicted in Table 5.1 and their integrated signals are displayed in Fig. 5.23-5.26 in the appendix. Table 5.1 also contains all reasonable molecular compositions based on the four elements C, H, N, and O, since the mass resolution of our mass spectrometer is not sufficient to disentangle isobaric species. As such, we cannot distinguish between different elemental compositions in one mass channel and only the pure carbon ($C_n{}^+$) and C_nH^+ species can be assigned unambiguously, whereas species of various $C_AN_BO_CH_D{}^+$ compositions are plausible for other mass channels as well.

The possible inclusion of nitrogen atoms in the fragment ions, as well as the reactivity of fragment ions towards background water (i.e. the inclusion of O-atoms in the molecule), complicate the analysis of the data. Hence, to facilitate the discussion on the evolution of species, we refer to the observed ionic species using the $\Gamma_n + \eta$ notation, where n signifies the number of heavy atoms in the ion ($C_AN_BO_CH_D{}^+$, $n = A + B + C$, Γ = C, N, O) and η the number of hydrogen equivalents in the ion. E.g. m/z 122, 123, and 124 will be referred to as $\Gamma_{10} + 2$, $\Gamma_{10} + 3$, $\Gamma_{10} + 4$, respectively. The pure carbon ions are used as reference points, with $\eta = 0$. The assignment of two independent variables to one mass channel allows us to group each observed mass peak in two different ways. To probe the stability of the fragments with respect to their size, we grouped the appearing fragments based on the number of heavy atoms (Γ_n). This method allows for a comparison of individual contributions within one Γ_n

Table 5.1: Ion signals in the m/z 103 – 199 range detected as a result of the photodissociation of **TAC**$^{\bullet+}$.

Identified masses (m/z)	Probable Compositions $C_AN_BO_CH_D$					Group Γ_n	Group η	Complete Notation Γ_n+η
108	C_9					Γ_9	0	Γ_9+0
109	C_9H						1	Γ_9+1
110	C_9H_2	C_8N					2	Γ_9+2
111	C_9H_3	C_8HN					3	Γ_9+3
112	C_9H_4	C_8H_2N	C_7N_2		C_8O		4	Γ_9+4
120	C_{10}					Γ_{10}	0	Γ_{10}+0
121	$C_{10}H$						1	Γ_{10}+1
122	$C_{10}H_2$	C_9N					2	Γ_{10}+2
123	$C_{10}H_3$	C_9HN					3	Γ_{10}+3
124	$C_{10}H_4$	C_9H_2N	C_8N_2		C_9O		4	Γ_{10}+4
125	$C_{10}H_5$	C_9H_3N	C_8HN_2		C_9HO		5	Γ_{10}+5
126	$C_{10}H_6$	C_9H_4N	$C_8H_2N_2$	C_7HN_3	C_9H_2O		6	Γ_{10}+6
127	$C_{10}H_7$	C_9H_5N	$C_8H_3N_2$	$C_7H_2N_3$	C_9H_3O		7	Γ_{10}+7
132	C_{11}					Γ_{11}	0	Γ_{11}+0
133	$C_{11}H$						1	Γ_{11}+1
134	$C_{11}H_2$	$C_{10}N$					2	Γ_{11}+2
135	$C_{11}H_3$	$C_{10}HN$					3	Γ_{11}+3
136	$C_{11}H_4$	$C_{10}H_2N$	C_9N_2		$C_{10}O$		4	Γ_{11}+4
144	C_{12}					Γ_{12}	0	Γ_{12}+0
145	$C_{12}H$						1	Γ_{12}+1
146	$C_{12}H_2$	$C_{11}N$					2	Γ_{12}+2
147	$C_{12}H_3$	$C_{11}HN$					3	Γ_{12}+3
148	$C_{12}H_4$	$C_{11}H_2N$	$C_{10}N_2$		$C_{11}O$		4	Γ_{12}+4

group. Moreover, it enables a cross comparison of the integrated signals of each Γ_n cluster (e.g. comparing intensities in Γ_9 and Γ_{10}). However, Γ_n alone does not allow us to probe how mass distributions change for different values of n. Fragments where a carbon atom is exchanged by a nitrogen atom shift their mass by two amu. Visualizing this shift highlights how the potential incorporation of heteroatoms changes with the cluster size Γ_n. To facilitate such a comparison we group the appearing masses according to their η-value. Each added amu raises its value by one until the next higher carbon mass is reached, allowing us to intuitively group mass peaks that have similar composition but a different number of heavy atoms.

The RF setting of our ion trap allows for a complete analysis down to the Γ_9 region and all the way up to the Γ_{12} region. To investigate the distribution of individual mass channels within the same cluster size as a function of fluence, we first grouped them based on their Γ_n-value, as illustrated in Fig. 5.5. The different groups show contrasting signals, demonstrating that the number of heavy atoms significantly influences the product distributions.

The Γ_9 group shows almost no signal for $\Gamma_9 + 0$ (which can only be the bare $C_9{}^+$ species) over the investigated range, whereas $\Gamma_9 + 1$ (C_9H^+) rises fast and is the most intense signal. $\Gamma_9 + 2$ has a similar intensity as $\Gamma_9 + 1$, but after peaking at around 8 pulses, it shows a significant decline by almost 60%, indicating that it is either being processed further at higher fluence or that its production is impeded due to other channels becoming more important. In contrast $\Gamma_9 + 3$ and $\Gamma_9 + 4$ are produced slightly slower and are less intense than the other two, but show no decline within our investigated region, which suggests that these correspond to more stable structures.

For Γ_{10} we observe fragments from $\eta = 0 - 7$, which is a clear deviation from all other groups. The appearance of fragments with η-values between 5 and 7 are only observed in significant quantities in this group, which can be explained by either retaining up to 7 hydrogen atoms in the fragment structure, by incorporating up to three nitrogen atoms, or by oxygen inclusion. The first two options would require unreasonable amounts of hydrogen and nitrogen atoms, that are in conflict with the observations in the previously discussed mass ranges. The high reactivity of $\mathbf{TACH}^+$ to form m/z 320 shows that reactions with water can happen readily in our ion trap, rendering the water addition reaction as the most likely candidate to explain these peaks.

We tried to prove the above hypothesis by gently raising the RF value so that the $\Gamma_9 + 1$ channel is no longer retained in the trap. As soon as retention of $\Gamma_9 + 1$ is no longer possible, the $\Gamma_{10} + 5$ to $\Gamma_{10} + 7$ peaks also disappear, which indicates that they are formed by chemistry involving $\Gamma_9 + 1$. This interpretation is also in line with similar findings in the literature during the dissociation of coronene (Panchagnula *et al.* 2024). Likely reaction candidates are C_9H, which can initially form m/z 127 (C_9H_3O) by reaction with water and lose up to two hydrogen atoms through photoprocessing forming masses m/z 125 (C_9HO). The potential loss of a hydrogen atom in C_9HO to form m/z 124 is not observed in the coronene measurements (Panchagnula *et al.* 2024). This reaction in the ion trap also masks the true $\Gamma_9 + 1$ signal. If we assume that $\Gamma_{10} + 5$ to $\Gamma_{10} + 7$ arise exclusively from the $C_9H + H_2O$ reaction, their combined intensities show a clear dominance of the $\Gamma_9 + 1$ channel in its group. Its overall fluence dependence does not change and only its maximum is pushed to slightly higher laser fluences.

The remaining signals in the Γ_{10} group show that $\Gamma_{10} + 0$ is dominant at high fluences, but grows in somewhat slower than $\Gamma_{10} + 3$, which is the second most intense channel. The three other channels, $\Gamma_{10} + 1$, $\Gamma_{10} + 2$, and $\Gamma_{10} + 4$ exhibit similar intensities but $\Gamma_{10} + 2$ is produced instantly, while $\Gamma_{10} + 1$ and $\Gamma_{10} + 4$ grow in around 5 pulses. Γ_{11} and Γ_{12} show very similar behavior, with similar intensities for all mass channels except for $\Gamma_{11} + 0$, which is the dominant signal within its group. All other masses from $\eta = 1 - 4$ are non-zero, but are significantly less intense than comparable signals from other Γ_n groups.

To quantify the stabilities of the various observed ionic fragments, we integrated ion signals in the respective groups and cross compared their intensities as a function of photon

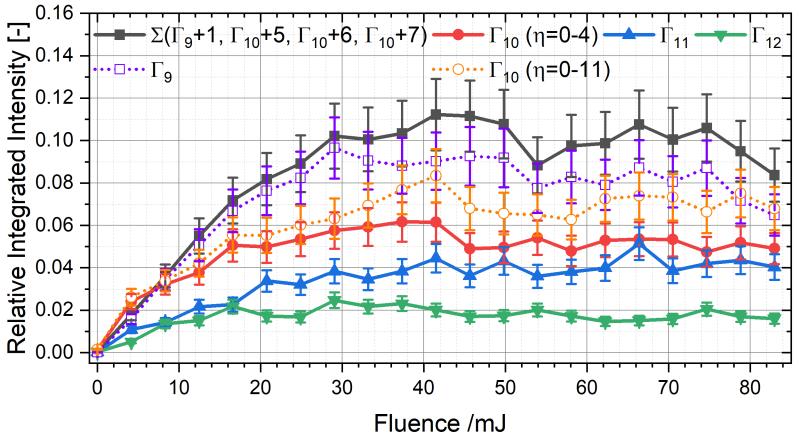

Figure 5.6: Integrated values of all observed peaks in the respective Γ_n sections. The original signal of $\Gamma_9 + 1$ (empty purple squares) was modified by adding the signals from $\Gamma_{10} + 5$, $\Gamma_{10} + 6$, and $\Gamma_{10} + 7$ due to the reaction of $\Gamma_9 + 1$ with water. Similarly, the original signal of Γ_{10} (empty orange dots) was modified by subtracting $\Gamma_{10} + 5$, $\Gamma_{10} + 6$, and $\Gamma_{10} + 7$.

fluence. Fig. 5.6 shows that Γ_9 clearly dominates, while Γ_{10} and Γ_{11} exhibit equal intensities, and Γ_{12} being the least intense of all. The intensities of Γ_9 are more than twice as high as Γ_{10} and Γ_{11}, which underlines the general trend that smaller fragments with fewer heavy atoms tend to be produced more efficiently than bigger ones. While all groups exhibit a rise within the first 8 pulses, Γ_{10}, Γ_{11}, and Γ_{12} plateau afterwards. In contrast Γ_9 begins to decline after reaching its maximum intensity. As such, even though Γ_9 is produced more efficiently it is processed further, whereas Γ_{10-12} seem to be more stable, due to their plateau.

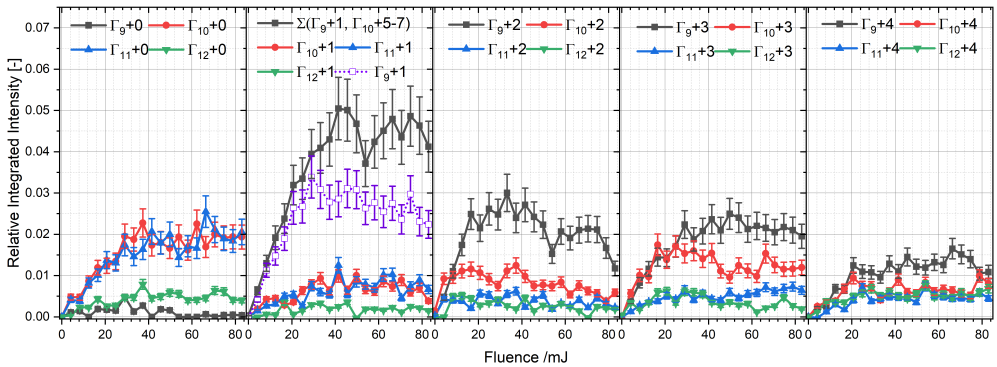

Figure 5.7: Photon flux dependence of individual mass peaks for $\eta = 0 - 4$. The original signal of $\Gamma_9 + 1$ (empty purple squares, dotted line) was modified by adding the signals from $\Gamma_{10} + 5$, $\Gamma_{10} + 6$, and $\Gamma_{10} + 7$ due to the reaction of $\Gamma_9 + 1$ with water.

Even though the Γ-value gives insight into the contributions of each mass in a group with the same number of heavy atoms as well as the fluence dependence of individual groups with different Γ_n, it is hard to determine how the product distribution changes depending on the cluster size. We therefore used the η-value to group signals with similar compositions but different number of heavy atoms and displayed their relative intensities as a function of laser fluence, as shown in Fig. 5.7. Pure carbon fragments ($\eta = 0$) do not appear with Γ_9 but only

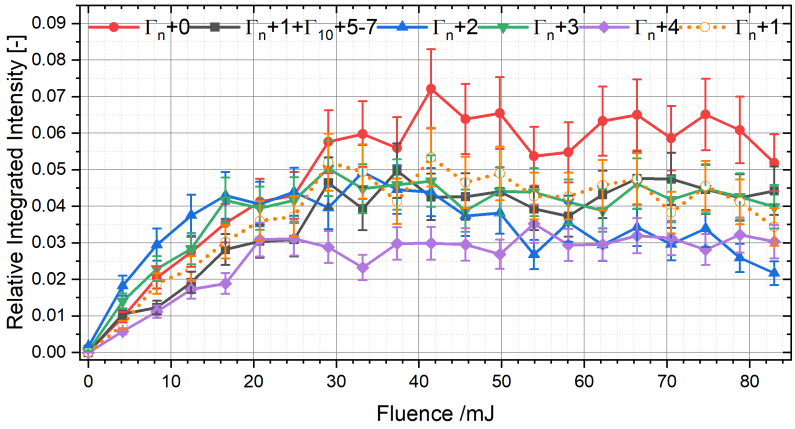

Figure 5.8: Integrated values of all observed peaks with the same η-value from Γ_9 to Γ_{12} for **TAC**$^{\bullet+}$. The original signal of $\Gamma_9 + 1$ (empty orange circles, dotted line) was modified by adding the signals from $\Gamma_{10} + 5$, $\Gamma_{10} + 6$, and $\Gamma_{10} + 7$ due to the reaction of $\Gamma_9 + 1$ with water.

form for Γ_{10} and higher. Here, $\Gamma_{10}+0$ and $\Gamma_{11}+0$ follow identical trends and exhibit the same intensities whereas $\Gamma_{12}+0$ is less intense. For $\eta = 1$, corresponding to the monohydrogenated carbon cluster (C_nH^+), the dominant signal is found for $\Gamma_9 + 1$, while the others are six times less abundant. The dominance of the Γ_9 region is also shown for $\eta = 2, 3$, although it is less pronounced there. In both groups the Γ_{10} fragments are (slightly) more intense than Γ_{11} and Γ_{12}, which are equally intense. This trend continues for $\eta = 4$ where all four mass channels exhibit very similar intensities and Γ_9 is only marginally more intense. As a result, while species with $\eta \leq 3$ do show some preference for smaller species with less heavy atoms, there is almost no preference for the size of a species when $\eta = 4$. The fluence dependence of each mass channel has already been described in detail for the Γ groups and no notable discrepancies arise within the new grouping.

To complete our analysis we cross compared the different η groups by integrating over all mass channels with the same η-value. Fig. 5.8 shows that $\Gamma_n + 1$ signals exhibit the highest intensities, with $\Gamma_n + 0$, $\Gamma_n + 2$, and $\Gamma_n + 3$ having comparable intensities over large portions of the investigated laser fluences. $\Gamma_n + 4$ has the slowest rise and least intensity at lower photon fluxes, yet the decay of the $\Gamma_n + 2$ group in the second half of our investigated range shows that both groups have comparable intensities. Contrary to Fig. 5.6, Fig. 5.8 shows that the fragments in the **TAC**$^{\bullet+}$ dissociation are distributed almost equally up to $\eta = 4$, and only due to the intense Γ_9+1 signal is the respective $\eta = 1$ channel slightly more intense.

5.4 Discussion

5.4.1 Differences between coronene and TAC

Coronene and **TAC** are isoelectronic and the only difference between the two structures is that three equidistant CH units in coronene are substituted with nitrogen atoms. The similarity allows us to gain insight into the dissociation mechanism as well as investigate the role that the exoskeletal ring plays in the formation of main fragment ions as compared to coronene. Before we can discuss these adequately, we need to first understand which photodissociation fragments are formed in the **TAC**$^{\bullet+}$ and coronene radical cation (**Cor**$^{\bullet+}$), respectively.

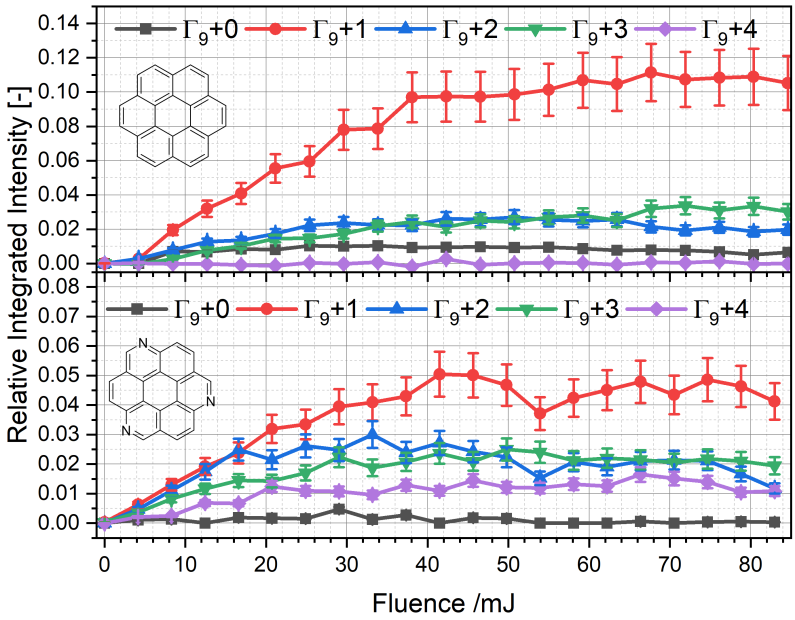

Figure 5.9: Comparison of the fragment ions formed in the dissociation of **Cor**$^{\bullet+}$ (top) and **TAC**$^{\bullet+}$ (bottom) in the mass range spanning m/z 108 to 112. The $\Gamma_9 + 1$ channels in both molecules are comprised of the initial $\Gamma_9 + 1$ signal as well as the $\Gamma_{10} + 5 - 7$ channels.

In **Cor**$^{\bullet+}$ dissociation the lower mass section is exclusively dominated by carbon clusters like $C_{10-14}{}^{+}$ or singly hydrogenated polyynes (C_9H^+), while in **TAC**$^{\bullet+}$ many more peaks are observed that cannot be attributed to these species. To better illustrate this behavior, Fig. 5.9 shows the relative integrated peak intensities of all observed Γ_9 fragments for **Cor**$^{\bullet+}$ (top) and **TAC**$^{\bullet+}$ (bottom). In both, the $\Gamma_9 + 1$ fragments are clearly dominating, while $\Gamma_9 + 2$, $\Gamma_9 + 3$ and $\Gamma_9 + 0$ exhibit smaller values. However, the relative strength of the $\Gamma_9 + 1$ channel with respect to the other channels is significantly higher in **Cor**$^{\bullet+}$ than in **TAC**$^{\bullet+}$, which suggests a more equal distribution of the observed fragments for Γ_9 in the latter. The fourth mass, $\Gamma_9 + 4$, is completely absent in **Cor**$^{\bullet+}$ dissociation, but visible in **TAC**$^{\bullet+}$. Its presence is one of the major differences between **Cor**$^{\bullet+}$ and **TAC**$^{\bullet+}$ and similar trends can be observed for Γ_{10-12}, as illustrated in Fig. 5.27-5.29.

Before we interpret this difference, we also want to point out that fragments in the Γ_{9-12} region appear to reach their maxima at lower pulse numbers for **TAC**$^{\bullet+}$, which is expected since the incorporation of nitrogen atoms into a PAH structure is associated with a reduced stability of the aromatic structure (Bouwman *et al.* 2015). The latter conclusion needs to be treated with care, as laser alignment differences between the two experiments may also induce slight differences.

The shift in the **TAC**$^{\bullet+}$ photoproducts towards higher η-values can be either attributed to the incorporation of nitrogen atoms forming $C_AN_{B=1,2}$ cations or by more hydrogen atoms leading to $C_AH_{D=2-4}$. The complete absence of any C_AH_4 ions in the **Cor**$^{\bullet+}$ experiments as well as the lower number of hydrogen atoms available in **TAC**$^{\bullet+}$ compared to **Cor**$^{\bullet+}$ (12 in **Cor**$^{\bullet+}$ and 9 in **TAC**$^{\bullet+}$) both point to nitrogen atom incorporation rather than the formation of carbon structures with extra hydrogen atoms. The nitrogen incorporation into **Cor**$^{\bullet+}$ therefore expresses itself by lowering the propensity to form pure carbonaceous fragments, while raising the availability of mixed C/N/H-bearing fragments. In this context it is also interesting to mention that there is no experimental evidence supporting the formation

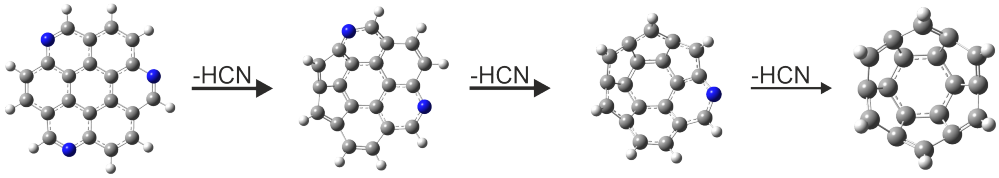

Figure 5.10: Possible HCN loss mechanisms for **TAC**.

of cationic fragments with three nitrogen atoms, suggesting that at least one nitrogen-atom is contained in the neutral co-fragment, or that structures with three nitrogen atoms are too high in energy and cannot be accessed.

The formation of nitrogenated cationic fragments seems obvious at first glance, considering that **TAC** has a C/N ratio of 7, and nitrogen atoms are distributed evenly over the molecular structure. Yet, previous studies showed that HCN elimination dominates for all investigated smaller PANHs (Bouwman *et al.* 2015; de Haas *et al.* 2017), and the only channel that has been shown to be able to compete with the HCN loss is hydrogen atom elimination (Bouwman *et al.* 2015). Consequently, literature data (Bouwman *et al.* 2015; de Haas *et al.* 2017) currently predict the exclusive appearance of completely carbonaceous fragments for $\mathbf{TAC}^{\bullet+}$. The latter are still detected as major products in our experiments with $\mathbf{TAC}^{\bullet+}$, which simultaneously highlights their stability and provides experimental evidence that multiple nitrogen atoms can be efficiently eliminated from larger PANH structures.

Now that we established which fragments appear in the $\mathbf{TAC}^{\bullet+}$ case, we aim to deduce a possible dissociation mechanism. The photoprocessing of $\mathbf{TAC}^{\bullet+}$ is initiated in two different ways, by either losing a hydrogen atom and forming $\mathbf{TAC}{-}\mathrm{H}^+$ or by loss of CNH_{1-3}. The former channel reacts to m/z 320 on the time scale of our experiment, while the latter leads to m/z 274−276 from where two possibilities exist for further decays. One can eliminate another HCN fragment to form m/z 247 leading to mono nitrogenated or even pure carbonaceous species and the other towards dicyanopolyynes ($\Gamma_n + 4$), by expulsion of these as the charge-bearing fragments. The fact that masses corresponding to just three CNH_{1-3} losses have only minor intensities indicates that this pathway is unfavorable and structures resulting from three HCN eliminations cannot be formed easily, ultimately resulting in the appearance of cyanopolyyne fragments ($\Gamma_n + 2$, $\Gamma_n + 3$).

From the data, it is inferred that the masses between m/z 220 and m/z 276 represent major branching points where nitrogen inclusion into cationic fragments is decided. We can try to visualize this mechanism by extrapolating from the dissociation mechanism of smaller PANHs. Recently, Subramani *et al.* (2023) showed that the dissociation of the quinoline cation exhibits its lowest energy pathway towards pentalene via elimination of a neutral HCN fragment. If one considers $\mathbf{TAC}^{\bullet+}$ to be three separate quinoline units, all three nitrogen atoms may be eliminated via HCN fragments, resulting in a open bowl structure, due to the introduction of five-membered rings in the outside rings of the initially planar $\mathbf{TAC}^{\bullet+}$ structure. Such a dissociation mechanism is depicted schematically in Fig. 5.10. However, to agree with the less intense signals from m/z 220 − 222, the third HCN fragment has to have a lower propensity to be eliminated. One possible explanation for this observation is increasing geometrical strain in the molecule with each HCN loss step. As a result, the energies of the transition states likely increases as well, which may also be why nitrogen elimination is not exclusively observed. Pure carbon fragments, like $\mathrm{C}_{11}{}^+$, are then formed from either m/z 247−249 or m/z 220−222 in accordance with the previously established PAH dissociation mechanisms. Based on these findings we come to the conclusion that once PANHs reach a low nitrogen content, their dissociation characteristics become very similar to regular PAHs. Contrary, a higher nitrogen content can lead to incorporation of nitrogen atoms into cationic photoproducts. Furthermore, the introduction of nitrogen atoms in the coronene

framework leads to an increased reactivity of key intermediates and different dissociation channels become more relevant.

The initial molecular transformations in PAH and PANH dissociation begin on the periphery of the molecule and so their shape and hetero atom substitution alter the dissociation mechanisms. In PAHs these effects have been investigated to some extend using experimental and computational techniques (Pla *et al.* 2021; Ekern *et al.* 1998; Rodriguez Castillo *et al.* 2018; Berné & Tielens 2012; Bouwman *et al.* 2016; Trinquier *et al.* 2017). Ekern *et al.* (1998) categorized PAHs when photodissociated using a Xenon arc lamp in four different groups: photostable, H-losses, H- and C-loss and completely photodestroyed. The main conclusion from their work is, that individual "exposed" aromatic rings are required in PAHs to see combined H- and C-losses. As such, highly symmetric PAHs, like the pericondensed coronene, show different dissociation patterns than irregular PAHs, like dibenzopyrenes. Our investigation of $\mathbf{TAC}^{\bullet+}$ offers the possibility to extend this phenomenological description to exoskeletal PANHs. Since the size of the PA(N)H can also affect its dissociation, we will only compare similar sized PAHs, like coronene and different dibenzopyrene ($C_{24}H_{14}$) isomers, to $\mathbf{TAC}^{\bullet+}$.

Even though $\mathbf{TAC}^{\bullet+}$ is a highly symmetrical PANH, the loss of small carbon fragments, like CNH_{1-3} is akin to the C_2/C_2H_2 losses in irregular PAHs. Hence, its dissociation pattern aligns best with that of an irregular, catacondensed PAHs like the dibenzopyrenes (DBPs). This observation can be best explained by considering that "exposed" aromatic rings in PAHs have a low photostability and are easily cleaved off (Ekern *et al.* 1998; Hrodmarsson *et al.* 2022). Similarly, nitrogen atom incorporation reduces the stability of aromatic rings (Bouwman *et al.* 2015), by acting as a breaking point in the molecular structure and facilitating the elimination of small carbonaceous fragments like HCN. As such, nitrogen containing rings, even in highly symmetric PANHs like $\mathbf{TAC}^{\bullet+}$, dissociate just like exposed rings in irregular PAHs resulting in their destruction and the occurrence of similar fragmentation patterns for both. However, these parallels reach their limits when looking at other photoproducts, like carbon clusters, the two differ substantially.

Further similarities between $\mathbf{TAC}^{\bullet+}$ and DBPs arise in their fragmentation mechanisms. Akin to our proposed formation of five-membered rings during the dissociation of $\mathbf{TAC}^{\bullet+}$ (see Fig. 5.10), Rodriguez Castillo *et al.* (2018) observed the formation of a five-membered ring species after molecular hydrogen loss in dibenzo[a,l]pyrene. This supports our proposed reaction mechanism in Fig. 5.10 and suggests that exoskeletal PANHs and irregular PAHs both favor connected structures, instead of "exposed" aromatic rings during their photoprocessing.

5.4.2 Astrophysical implications

Nitrogen containing polyynes like HC_nN, C_nN, and NC_nN chains have already been detected in the atmosphere of Titan as well as in the coma of the comet 67P/Churyumov-Gerasimenko (Bell *et al.* 1997; Mathé *et al.* 2018; Hänni *et al.* 2021). They are also suggested to be abundant in interstellar objects (Khanna *et al.* 1987; Petrie *et al.* 2003), but the absence of a dipole moment makes it hard to identify dicyanopolyynes. Recently Agúndez *et al.* (2023) proposed the presence of NC_4N in the dark molecular cloud TMC-1, based on the detection of its protonated derivative NC_4NH^+, providing first observational prove of their existence in the ISM. Another congener HC_5NH^+ has been detected tentatively (Marcelino *et al.* 2020) and even though no cationic (di)cyanopolyyne has been detected yet, their presence is expected as their neutral counterparts have been detected. So far the origin of these molecules is thought to be from bottom-up chemistry (Kostko *et al.* 2010; Grösser & Hirsch 1993; Cherchneff *et al.* 1993). The results presented here show that, among others, cyanopolyynes and dicyanopolyyne cations are likely created in the top-down photoprocessing of a PANH species.

In this context, their presence could help to evaluate the current predictions on nitrogen atom incorporation in PAHs. Based on current observations and shifts of the aromatic IR (AIR) bands, the amount of endoskeletal nitrogen atoms incorporated into the PAH framework has been suggested to be no more than 12% (Ricca *et al.* 2021). This estimate originates from the fact that endoskeletal PANHs exhibit an intense 11 μm band, which acts as a limiting factor. This feature is significantly reduced in regular PAHs as well as exoskeletal PANHs. Furthermore, exoskeletal CH/N substitutions alter the IR emission properties only marginally, if at all, making it almost impossible to discern between the two by IR observations alone. The number of nitrogen atoms that could be incorporated is also unclear and can hardly be identified by the aforementioned observational techniques. Photoproduct analysis could act as a more robust metric to determine the degree of nitrogen incorporation, independent from the AIR bands. Of course the difficulty to detect dicyanopolyynes also excludes them from being suitable tracers. However, our experiments show that the photoprocessing of $\mathbf{TAC}^{\bullet+}$ generates equal amounts of $\Gamma_n + 0$, and $\Gamma_n + 3$, while $\Gamma_n + 1$ is about 30% higher and $\Gamma_n + 2$ as well as $\Gamma_n + 4$, i.e. dicyanopolyynes, are approximately 30% less abundant (see Fig. 5.8). Although we cannot distinguish between nitrogen incorporation and additional hydrogen atoms in the detected fragments, it is likely that nitrogen atoms are also incorporated in the $\Gamma_n + 2$ and $\Gamma_n + 3$ channels. The resulting presence of cyano- (NC_n) and hydrocyanopolyynes (NC_nH), which both exhibit dipole moments, could potentially serve as a suitable tracer to estimate the degree of nitrogen incorporation in interstellar PAHs. This should lead to an upper limit, since the bottom-up production of these species represents a competing pathway. Future observations could actively search for cationic cyanopolyynes in the boundary layers between photon dominated regions and dark molecular clouds and determine their column densities to get a more reliable picture as to how common nitrogen atom incorporation in PAHs actually is.

5.5 Conclusion

We have investigated the photodissociation of a model PANH, $\mathbf{TAC}^{\bullet+}$ by simulating the continued photodissociation that occurs in photon dominated regions in space. The cations were retained in a Paul-Type ion-trap and irradiated using 630 nm photons from a dye laser. The photoproducts were subsequently ejected into a time-of-flight mass spectrometer and mass analyzed. $\mathbf{TAC}^{\bullet+}$ initially loses hydrogen atoms as well as up to three CNH_{1-3} fragments, while at lower m/z-values carbon based fragments appear that are accompanied by peaks with up to four hydrogen equivalents. Even though our setup cannot discriminate isobaric fragments, the presence of masses with three and four hydrogen equivalents in $\mathbf{TAC}^{\bullet+}$ and their complete absence in coronene demonstrates, that nitrogen atoms are also incorporated into these fragments. The size stability of the fragments suggests that masses below 10 heavy atoms are favored in the dissociation and double nitrogen incorporation is slightly less intense than single nitrogen or even pure carbon fragments. The dissociation mechanism is best described by a curl up of the planar PANH sheet from which cationic fragments are consequently ejected. The increasing rigidity of the intermediates likely impedes the elimination of the second and third HCN fragments, which may be the reason why nitrogen incorporation into lower mass fragments is observed. The dissociation characteristics of $\mathbf{TAC}^{\bullet+}$ can be best compared to that of an irregular PAH and consequently nitrogen-containing rings can be viewed similarly to "exposed" carbon rings in catacondensed PAHs. Both structural elements can be considered prominent breaking points in the molecular structure during their respective dissociation. The appearance of carbon fragments with one or two nitrogen atoms, shows that these species are formed in the dissociation of PANHs, which can ultimately help to determine the total nitrogen content in extraterrestrial PANHs.

Acknowledgements

JB acknowledges the Netherlands Organisation for Scientific Research (Nederlandse Organisatie voor Wetenschappelijk Onderzoek, NWO) for a Vidi grant (grant number 723.016.006). This work was supported in part by NASA's Solar System Exploration Research Virtual Institute (SSERVI): Institute for Modeling Plasma, Atmosphere, and Cosmic Dust (IMPACT). DS acknowledges support by the PRIME programme of the German Academic Exchange Service (DAAD) with funds from the German Federal Ministry of Education and Research (BMBF). DS ackowledges a grant for computing time at the Paderborn Center for Parallel Computing PC^2 under the project PEPICON. DS gratefully acknowledges continued support by Prof. Tina Kasper and funding from DFG under project number KA 3871/3-2 and 270672969.

5.A Appendices

These appendices contain further information to chapter 5. First, a description on the synthetic procedures to obtain **TAC** is given. Next, we present an example of Pearson IV fitted experimental data and the residual between experiment and fit. Also, the reaction of $\mathbf{TAC}^{\bullet+}$ with acetylene (C_2H_2) is presented. We show a zoom-in of the hydrogen loss region from $\mathbf{TAC}^{\bullet+}$ and show that m/z 320 does not dissociate in our experimental conditions. Lastly, we present the integrated intensities off all peaks and the comparison of $\mathbf{Cor}^{\bullet+}$ to $\mathbf{TAC}^{\bullet+}$ dissociation for the Γ regions not presented in chapter 5.

5.A.1 Synthetic procedures of TAC

5.A.1.1 Experimental

Chemical reagents were purchased from commercial suppliers and used without further purification. Flash column chromatography was performed on silica gel 60 Å (0.04 – 0.063 mm, Screening Devices B.V.). Thin Layer Chromatography (TLC) was performed on TLC Silica gel 60 plates (Kieselgel F254, Merck). NMR spectra was recorded on a Bruker AV-300 NMR or a Bruker AV-500 NMR instrument. Chemical shifts are given in ppm (δ) relative to the solvent signals. Mass spectrometry was performed on a Thermo Scientific LCQ Fleet spectrometer equipped with an electrospray ion source in positive ion mode. Elemental analysis was performed by Mikroanalytisches Labor Kolbe (c/o Fraunhofer Institut UMSICHT).

5.A.1.2 1,5,9-trinitrotriphenylene synthesis

To a solution of 2,3-dichloronitrobenzene (17.7 g, 92.2 mmol, 1 eq) in DMF (142 ml) was added copper powder (35.1 g, 553 mmol, 6 eq). The mixture was stirred at reflux for 19 h under N_2 atmosphere. After cooling to 120 °C, the hot solution was filtered over celite and the product was extracted from the celite with DMF (3 × 25 ml). The filtrate was then slowly poured into 6% ammonium solution (720 ml) (diluted from 18% NH3·H_2O (240 ml)) with vigorous stirring. The obtained black precipitate was collected by filtration and sequentially washed with diluted ammonium solution (48 ml) and water (48 ml). The obtained residue was then concentrated onto celite and purified using silica column chromatography (pentane : DCM, $2:1 \rightarrow 1:1$) to obtain a yellow solid (4.74 g, 13.0 mmol, 42%).
^{1}H NMR (300 MHz, $CDCl_3$) δ 8.21 (dd, J = 8.3, 1.2 Hz, 3H), 7.82 (dd, J = 8.1, 1.2 Hz, 3H), 7.60 (t, J = 8.2 Hz, 3H).
^{13}C NMR (75 MHz, $CDCl_3$) δ 148.51, 135.26, 135.00, 130.70, 130.26, 123.70.

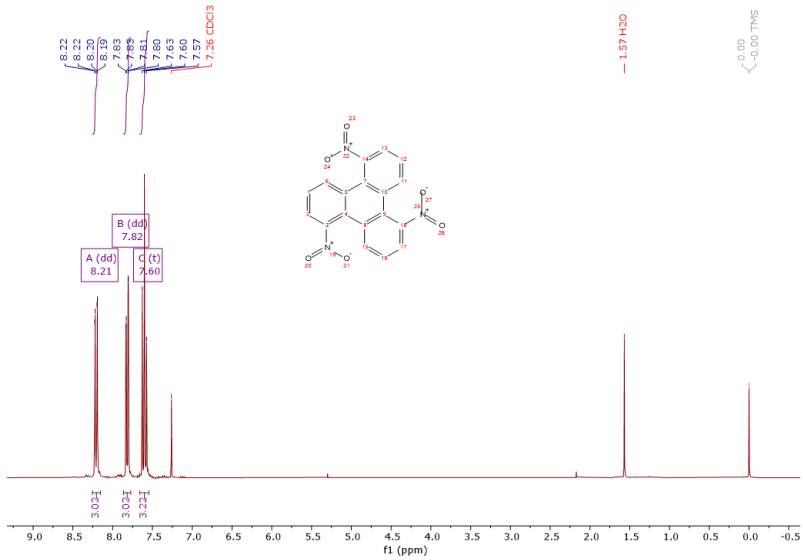

Figure 5.11: ^{1}H NMR spectrum of 1,5,9-trinitrotriphenylene.

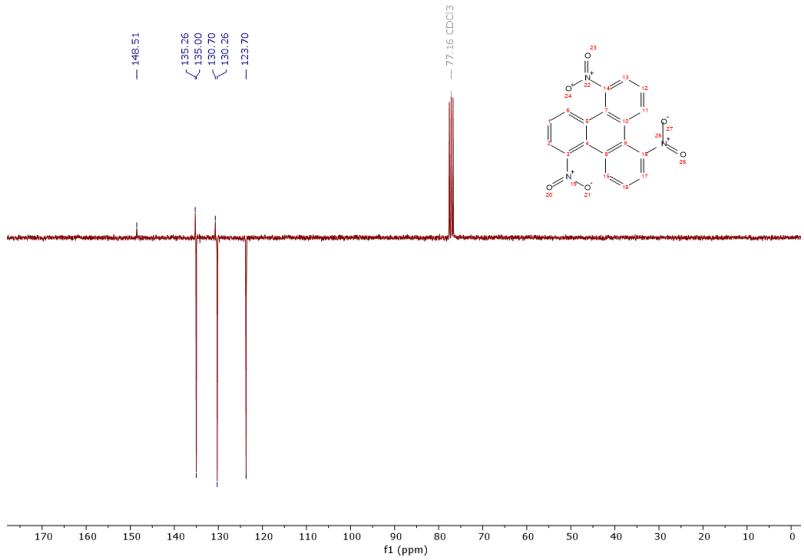

Figure 5.12: ^{13}C NMR spectrum of 1,5,9-trinitrotriphenylene.

5.A.1.3 Triphenylene-1,5,9-triamine synthesis

1,5,9-trinitrotriphenylene (3.0 g, 8.3 mmol, 1 eq) was dissolved in THF/MeOH (4:1, v/v, 80 ml). $Ni(OAc)_2{\cdot}4H_2O$ (2.0 g, 8.3 mmol, 1 eq) was added and the mixture was stirred for 5 min. Then, $NaBH_4$ (4.7 g, 124 mmol, 15 eq) was added in portions to the reaction mixture over 20 min and the obtained black mixture was stirred for an additional 15 min. Then, water was added (40 ml) and the mixture was filtered. The obtained residue was additionally washed with DCM/MeOH (200 ml), and the combined filtrate was evaporated under reduced pressure. Purification using silica column chromatography (0.1% MeOH in DCM) yielded a light-brown solid (1.2 g, 4.4 mmol, 52%).
^{1}H NMR (500 MHz, $CDCl_3$) δ 8.31 (dd, J = 8.1, 1.2 Hz, 3H), 7.25 (t, J = 7.9 Hz, 3H), 6.82 (dd, J = 7.8, 1.2 Hz, 3H), 4.31 (s, 6H).
^{13}C NMR (126 MHz, $CDCl_3$) δ 144.56, 132.23, 126.70, 119.42, 115.70, 115.43.
ESI-MS: m/z calcd for $C_{18}H_{16}N_3$ $[M+H]^+$ 274.13, found 274.08.

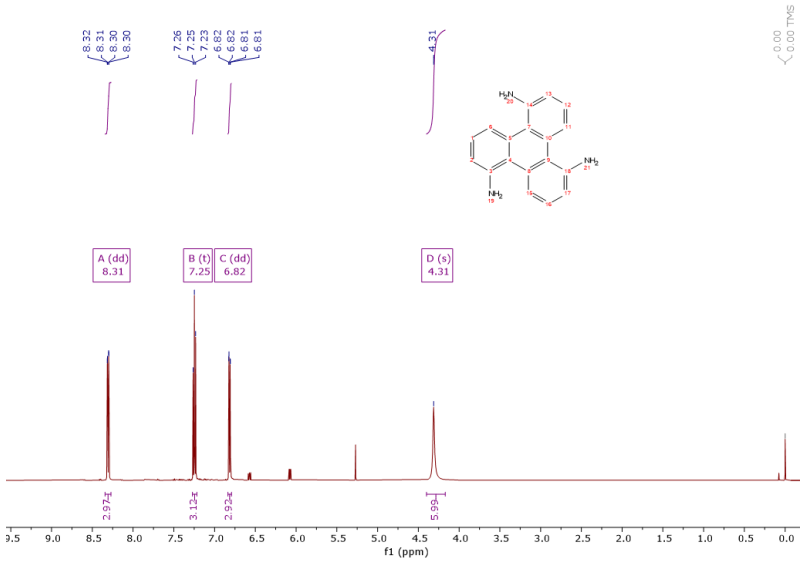

Figure 5.13: ^{1}H NMR spectrum of triphenylene-1,5,9-triamine.

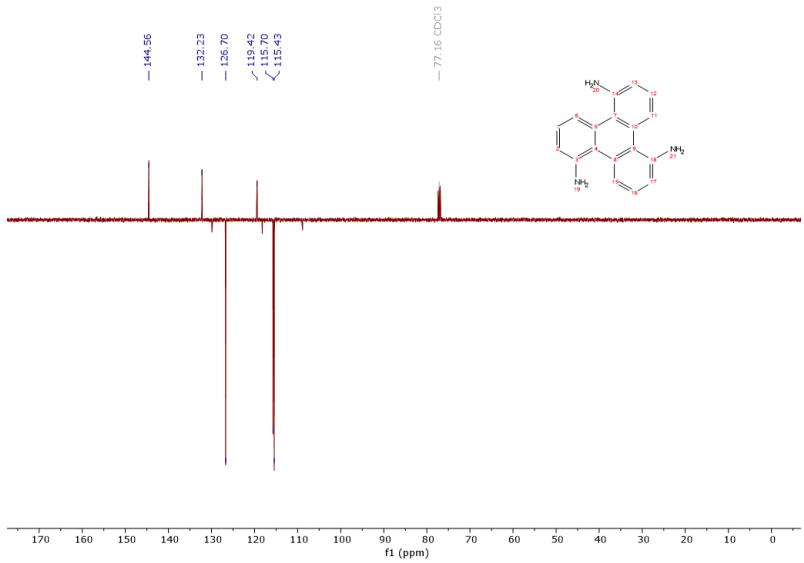

Figure 5.14: ^{13}C NMR spectrum of triphenylene-1,5,9-triamine.

5.A.1.4 N,N',N"-(triphenylene-1,5,9-triyl)triformamide synthesis

Formic acid (0.37 ml, 9.7 mmol, 5.3 eq) was added to a solution of acetic anhydride (0.73 ml, 7.7 mmol, 4.2 eq) at 0 °C. The mixture was heated to 50 °C and stirred for 2 h. After cooling the prepared mixture back down to 0 °C, a solution of the triphenylene-1,5,9-triamine (500 mg, 1.8 mmol, 1 eq) in THF (10 ml) was added dropwise over 15 min. Then, the reaction mixture was allowed to warm to room temperature and stirred for 18 h. The resulting precipitate was filtered, rinsed with ethyl acetate, and dried to afford pure product as a gray solid (591 mg, 1.7 mmol, 90%).
^{1}H NMR (500 MHz, DMSO-d6) δ 10.43 – 10.29 (m, 3H), 8.70 – 8.55 (m, 3H), 8.43 – 8.32 (m, 3H), 7.69 – 7.59 (m, 2H), 7.59 – 7.48 (m, 3H), 7.45 (t, J = 7.6 Hz, 1H).
^{13}C NMR (126 MHz, DMSO-d6) δ 164.04, 160.38, 133.90, 132.74, 132.67, 130.24, 126.88, 126.67, 126.50, 125.78, 125.74, 125.58, 125.49, 124.18, 124.03, 123.85, 123.70.
ESI-MS: calcd for $C_{21}H_{16}N_3O_3$ $[M+H]^+$ 358.12, found 358.08; $C_{21}H_{19}N_4O_3$ $[M+NH_4]^+$ 375.15, found 375.08.

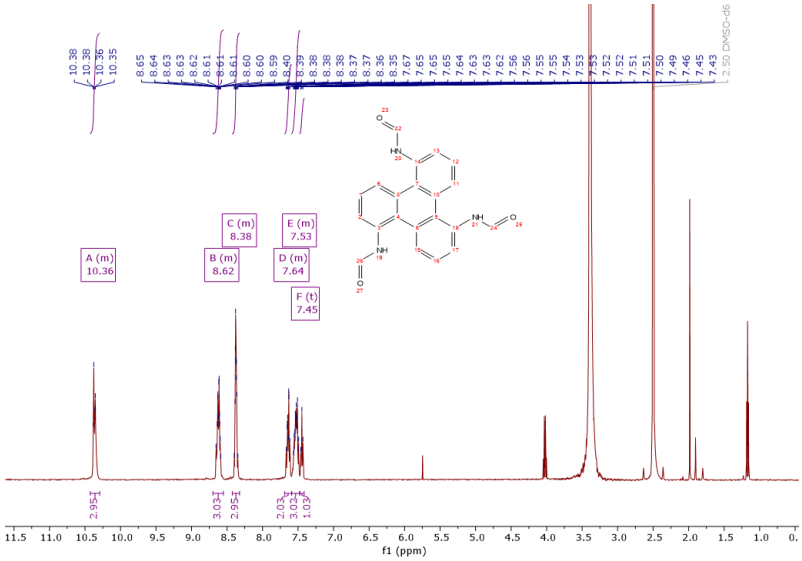

Figure 5.15: ^{1}H NMR spectrum of N,N',N"-(triphenylene-1,5,9-triyl)triformamide.

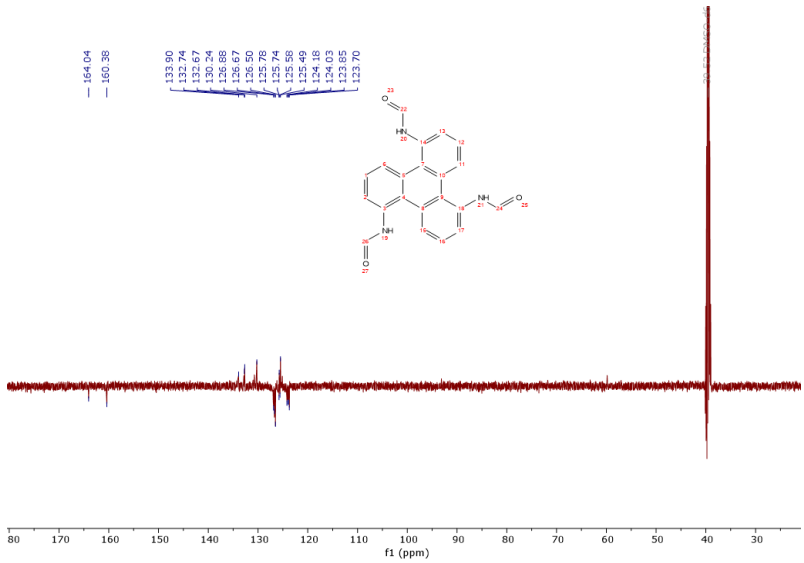

Figure 5.16: ^{13}C NMR spectrum of N,N',N"-(triphenylene-1,5,9-triyl)triformamide.

5.A.1.5 1,5,9-triazocoronene synthesis

A microwave vial was charged with N,N',N"-(Triphenylene-1,5,9-triyl)triformamide (0.50 g, 1.4 mmol, 1 eq), NaCl (4.1 g, 31 mmol, 22 eq) and $AlCl_3$ (4.1 g, 94 mmol, 67 eq) and purged with Ar. The mixture was heated to 230 °C and stirred for 4 h. After cooling to RT, the solids were stirred overnight in 15% aqueous NaOH (15 ml). The obtained yellow slurry was filtered over celite and washed with water (50 ml). The product dispersed in celite was dissolved in copious amounts of DCM/MeOH 10:1 until the filtrate was no longer yellow. The filtrate was evaporated under reduced pressure and washed with hot DCM/MeOH 10:1 (20 ml). The residue was collected by centrifugation to obtain product as brown-yellow solid (120 mg, 0.40 mmol, 23%).
^{1}H NMR (500 MHz, TFA) δ 11.38 (s, 3H), 10.12 (d, J = 8.9 Hz, 3H), 9.91 (d, J = 8.9 Hz, 3H).
^{13}C NMR (126 MHz, TFA) δ 155.15, 141.04, 138.61, 129.89, 126.93, 125.17, 118.36.
ESI-MS: m/z calcd for $C_{21}H_{10}N_3$ [M+H]+ 304.09, found 304.17.
Anal. Calcd for $C_{21}H_9N_3$: C, 83.16; H, 2.99; N, 13.85. Found: C, 83.09; H, 3.02; N, 13.81.

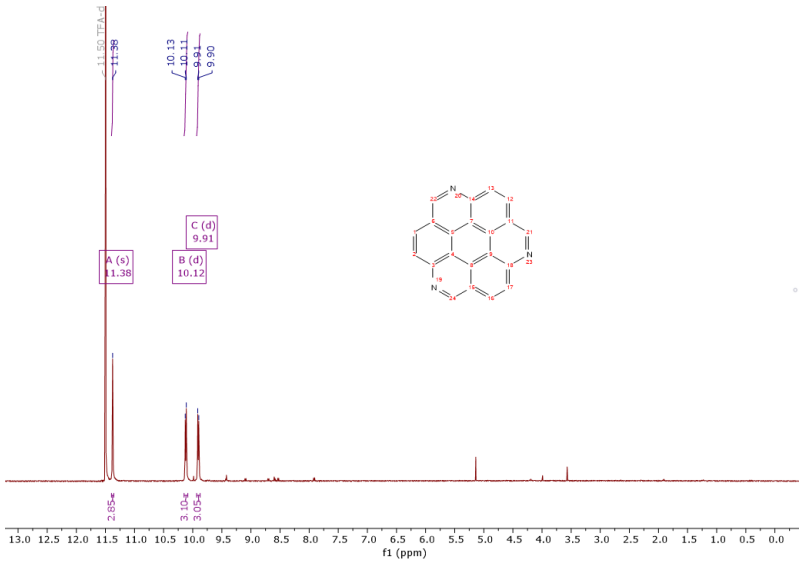

Figure 5.17: ^{1}H NMR spectrum of 1,5,9-triazocoronene.

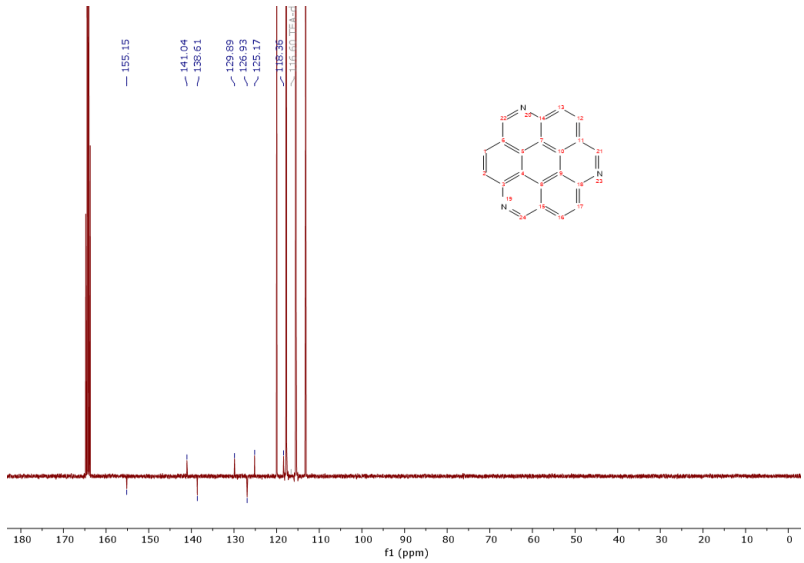

Figure 5.18: ^{13}C NMR spectrum of 1,5,9-triazocoronene.

5.A.2 Example of Pearson IV fitted experimental data and its residual

Here, we present an example of Pearson IV fitted experimental data and the residual between experiment and fit. This fitting procedure is used to find the integrated intensities of all peaks throughout chapter 5.

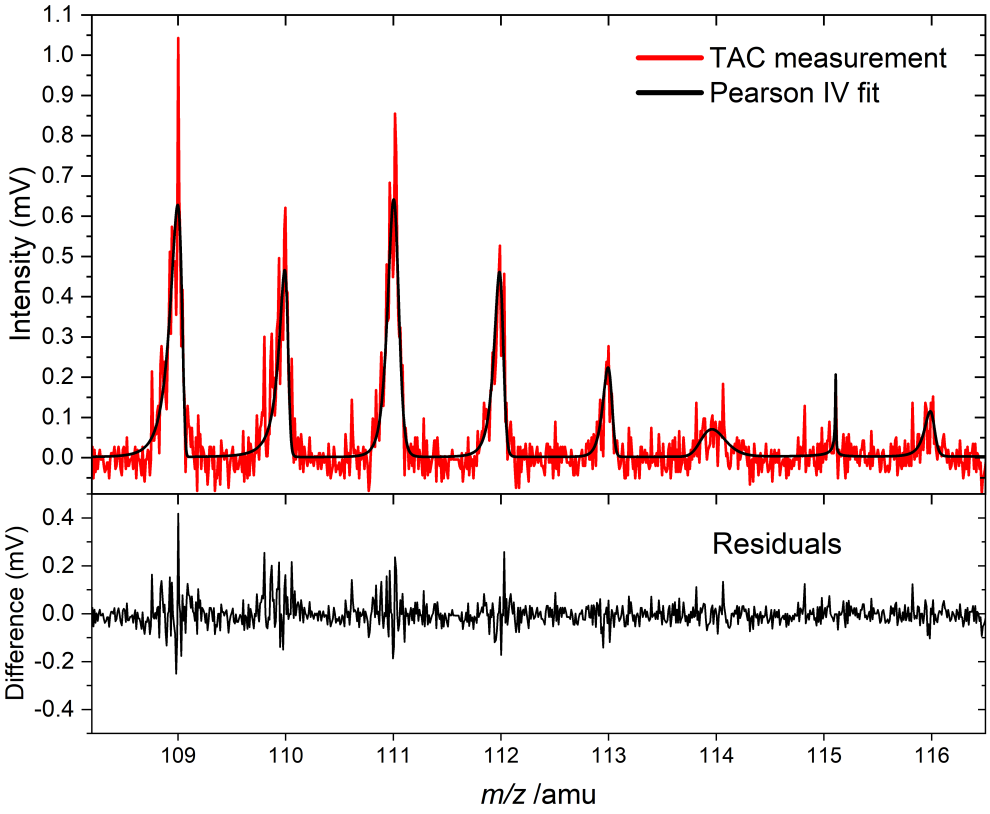

Figure 5.19: Top: Example of experimental data and fitted peaks used for integration. Bottom: Residuals between experiment and fit.

5.A.3 $\mathbf{TAC^{\bullet+}}$ reactivity with acetylene ($\mathbf{C_2H_2}$)

Here, the reaction of $\mathbf{TAC^{\bullet+}}$ with acetylene (C_2H_2) is presented. This indicates the high reactivity of $\mathbf{[TAC{-}H]^+}$, as it can react with both water and acetylene. Likely, the intensity of the acetylene addition species (m/z 328) is higher than the water addition species (m/z 320) due to the higher concentration of acetylene with respect to water, and not an increased reactivity of $\mathbf{[TAC{-}H]^+}$ with acetylene.

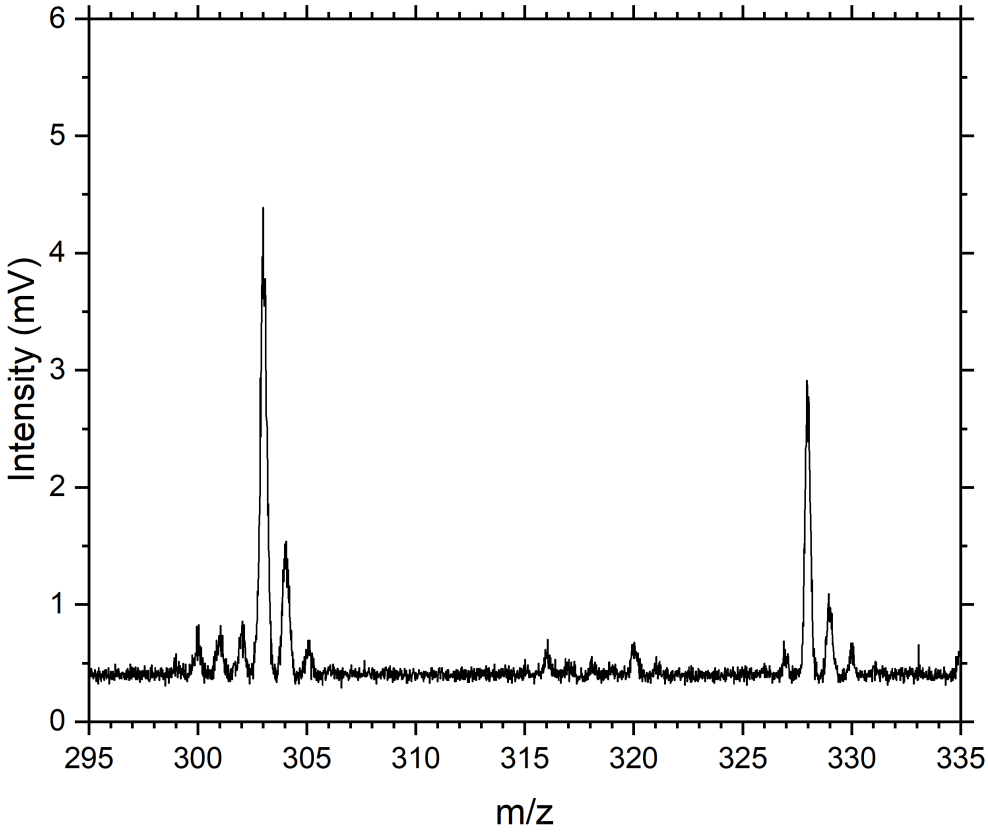

Figure 5.20: Mass spectrum of $\mathbf{TAC^{\bullet+}}$ dissociation with a mix of 5% acetylene instead of pure helium. The water addition product (m/z 320) is almost completely replaced by the acetylene addition product (m/z 328).

5.A.4 Zoom-in of the hydrogen loss region from TAC$^{\bullet+}$

Here, we show a zoom-in of the hydrogen loss region from **TAC**$^{\bullet+}$. Barely any hydrogen losses are observed, likely due to the high reactivity of these species with water.

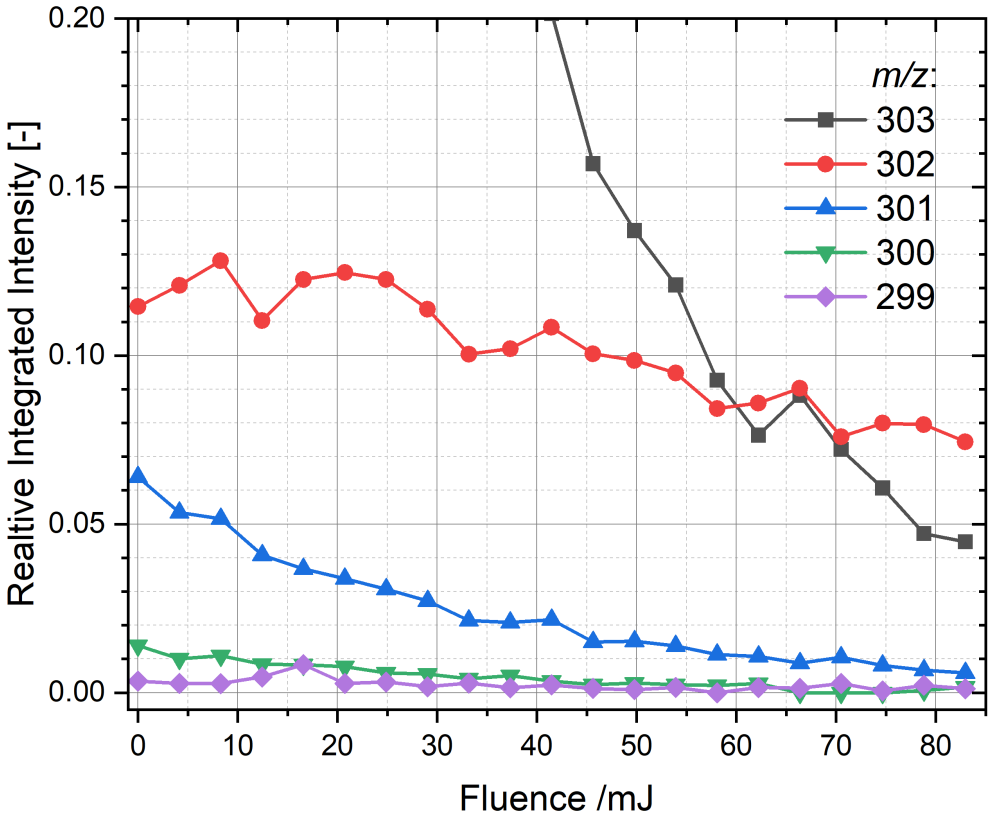

Figure 5.21: Zoomed-in view of the hydrogen loss region from **TAC**$^{\bullet+}$. No significant hydrogen losses are observed.

5.A.5 Dissociation mass spectra for m/z 320

Here, we present the dissociation of water addition species m/z 320 in our experimental conditions. Interestingly, no dissociation of this species was observed.

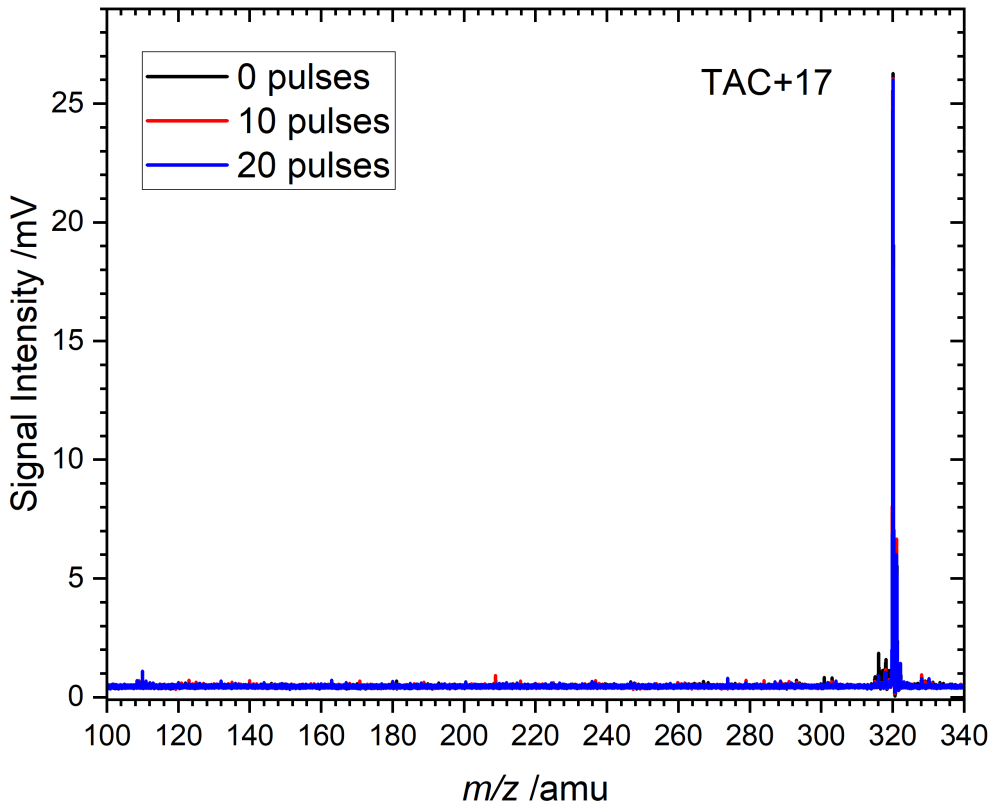

Figure 5.22: Dissociation mass spectra for m/z 320. No dissociation is observed.

5.A.6 Integrated intensities of all peaks from the Γ_{9-12} regions

Here, we present the integrated intensities of all peaks from the Γ_{9-12} regions. Several of these integrated intensities were already shown in Fig. 5.5 and 5.7.

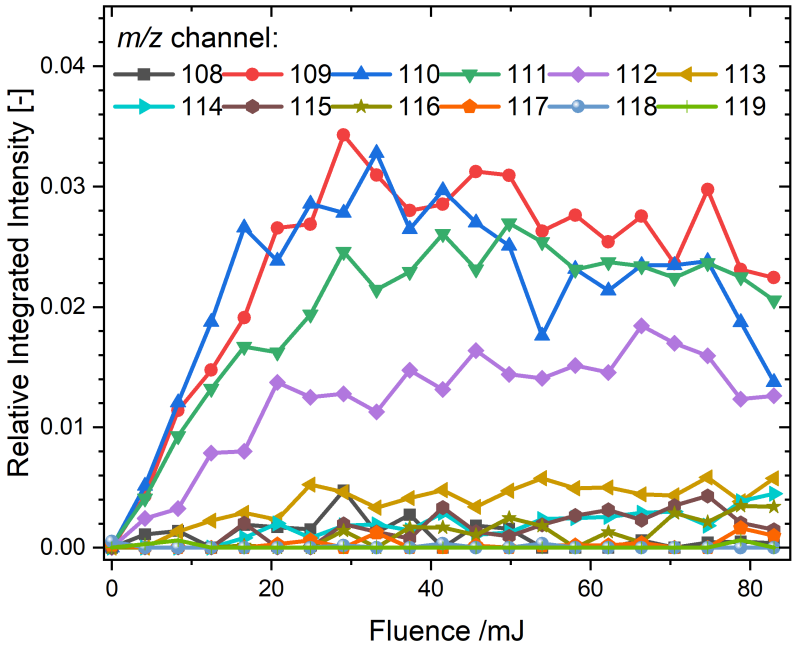

Figure 5.23: Integrated Intensities of all mass peaks in the Γ_9 region.

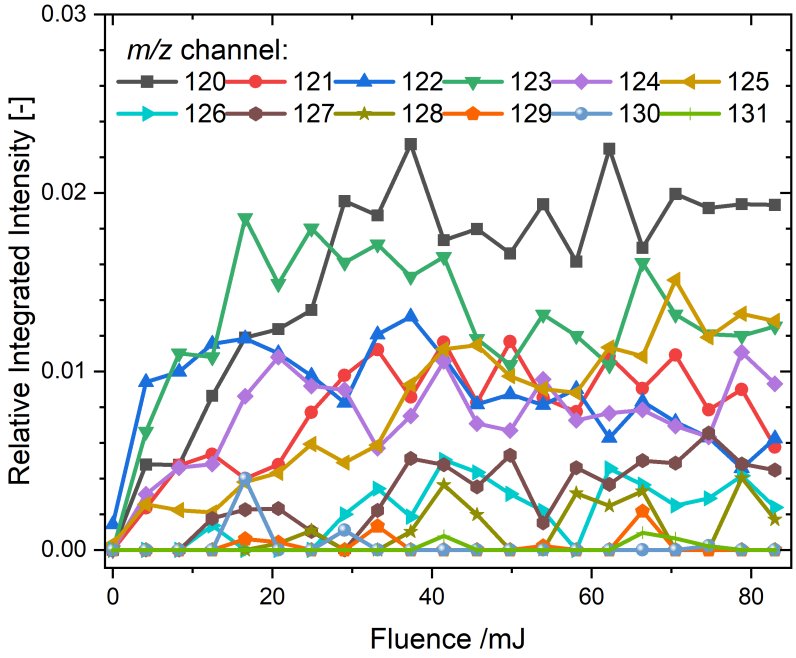

Figure 5.24: Integrated Intensities of all mass peaks in the Γ_{10} region.

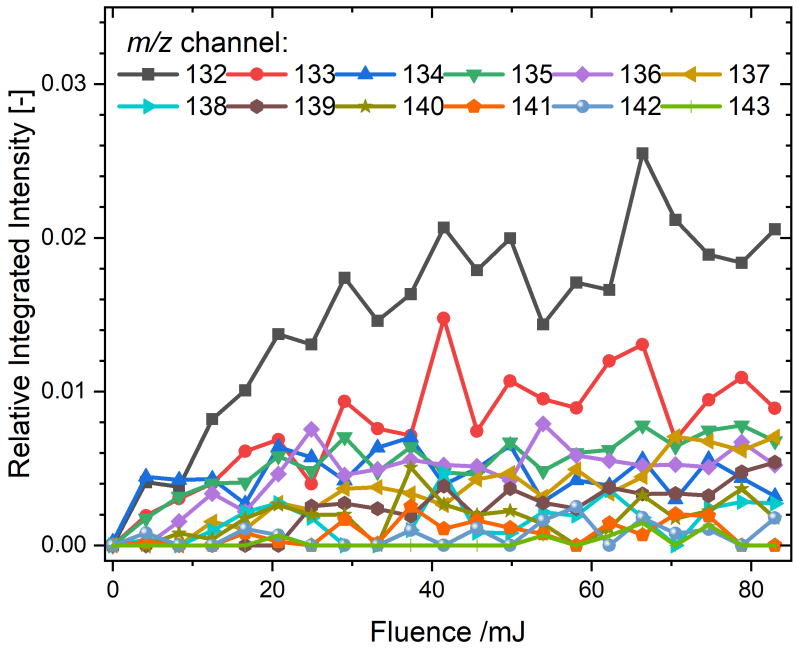

Figure 5.25: Integrated Intensities of all mass peaks in the Γ_{11} region.

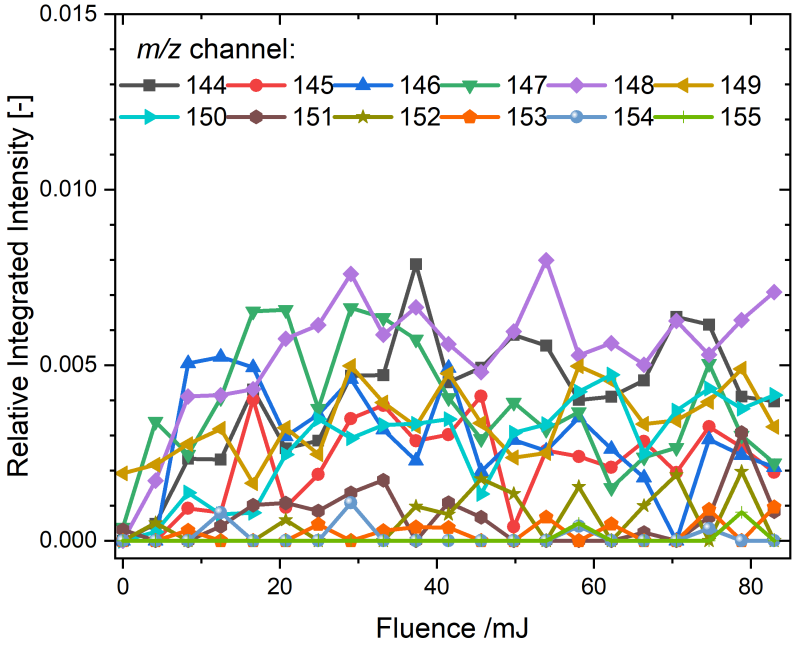

Figure 5.26: Integrated Intensities of all mass peaks in the Γ_{12} region.

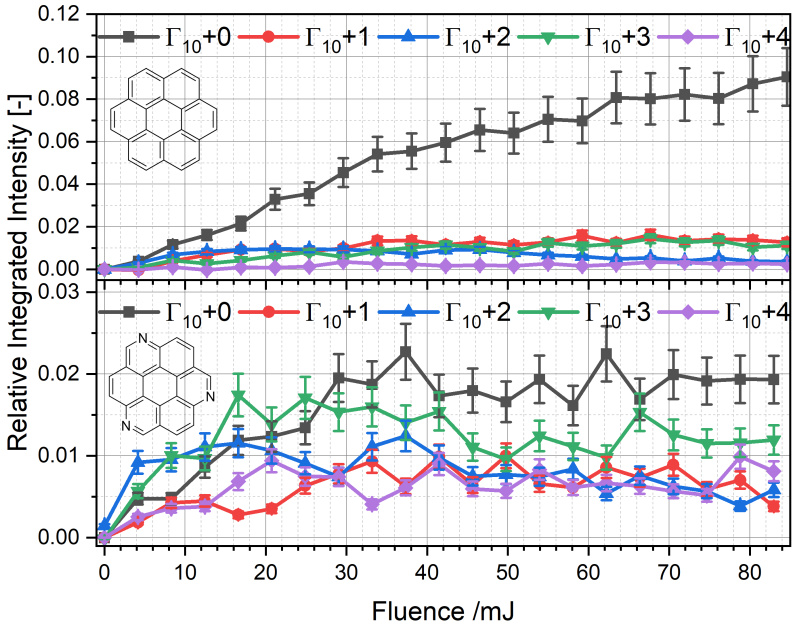

Figure 5.27: Integrated mass peaks for the Γ_{10} region for **Cor**$^{\bullet+}$ (top) and **TAC**$^{\bullet+}$ (bottom).

5.A.7 Cor$^{\bullet+}$ to TAC$^{\bullet+}$ comparison for the Γ_{10-12} regions

Here, we present the **Cor**$^{\bullet+}$ to **TAC**$^{\bullet+}$ comparison for the Γ_{10-12} regions. The comparison for the Γ_9 region can be found in Fig. 5.9

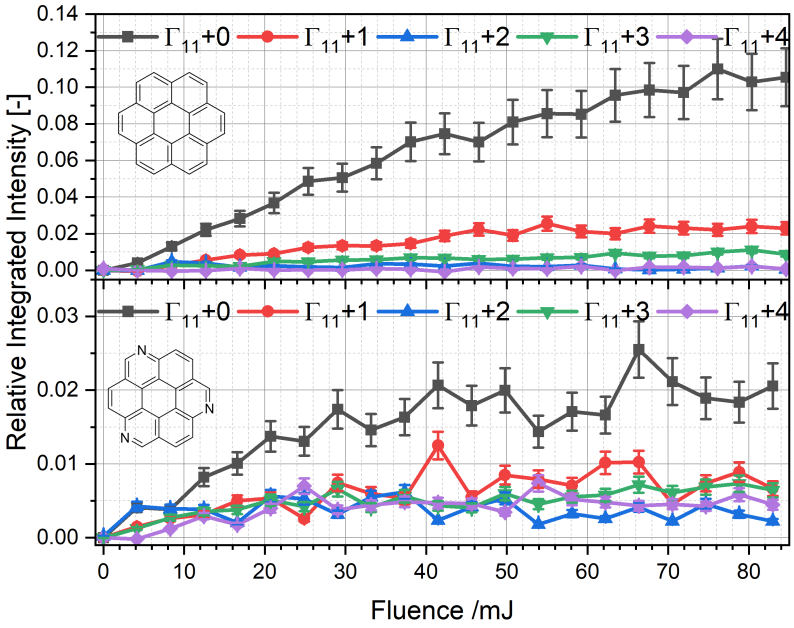

Figure 5.28: Integrated mass peaks for the Γ_{11} region for $\mathbf{Cor}^{\bullet+}$ (top) and $\mathbf{TAC}^{\bullet+}$ (bottom).

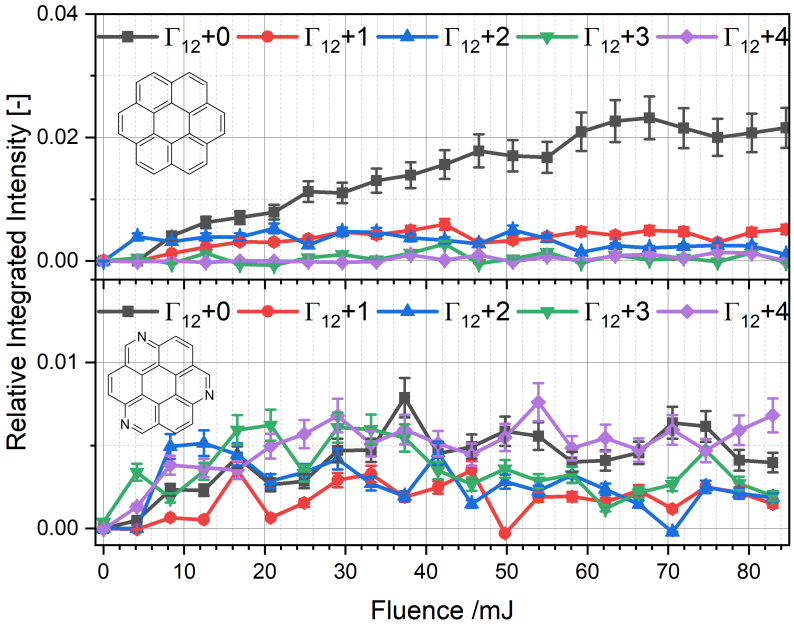

Figure 5.29: Integrated mass peaks for the Γ_{12} region for $\mathbf{Cor}^{\bullet+}$ (top) and $\mathbf{TAC}^{\bullet+}$ (bottom).